RESEARCH ARTICLE

NANO · MICRO small
www.small-journal.com

Cell Adhesion and Local Cytokine Control on Protein-Functionalized PNIPAM-co-AAc Hydrogel Microcarriers

*Sebastian Bernhard Rauer, Lucas Stüwe, Lea Steinbeck, Marcelo Augusto Szymanski de Toledo, Gereon Fischer, Simon Wennemaring, Jonas Marschick, Steffen Koschmieder, Matthias Wessling, and John Linkhorst**

Achieving adequate cell densities remains a major challenge in establishing economic biotechnological and biomedical processes. A possible remedy is microcarrier-based cultivation in stirred-tank bioreactors (STBR), which offers a high surface-to-volume ratio, appropriate process control, and scalability. However, despite their potential, commercial microcarriers are currently limited to material systems featuring unnatural mechanical properties and low adaptability. Because matrix stiffness and ligand presentation impact phenotypical attributes, differentiation potential, and genetic stability, biotechnological processes can significantly benefit from microcarrier systems tailorable toward cell-type specific requirements. This study introduces hydrogel particles co-polymerized from poly(N-isopropylacrylamide) (PNIPAM) and acrylic acid (AAc) as a platform technology for cell expansion. The resulting microcarriers exhibit an adjustable extracellular matrix-like softness, an adaptable gel charge, and functional carboxyl groups, allowing electrostatic and covalent coupling of cell adhesive and cell fate-modulating proteins. These features enable the attachment and growth of L929 mouse fibroblast cells in static microtiter plates and dynamic STBR cultivations while also providing vital growth factors, such as interleukin-3, to myeloblast-like 32D cells over 20 days of cultivation. The study explores the effects of different educt compositions on cell-particle interactions and reveals that PNIPAM-co-AAc microcarriers can provide both covalently coupled and diffusively released cytokine to adjacent cells.

1. Introduction

Anchorage-dependent cells play a pivotal role in a variety of industrial-relevant biotechnological processes ranging from the well-established production of biologicals and pharmaceuticals to early-stage applications such as cultured meat, cell therapy, or tissue engineering.[1–4] However, despite their success as production vessels for recombinant proteins, monoclonal antibodies, viral vectors and vaccines,[5–9] achieving adequate cell densities of desired cellular viability, functionality, and potency remains a significant challenge on the way toward industrialization and commercialization of laboratory-grown meat and medical therapies.[10,11] While *in vitro* meat production is estimated to require 10^{14} cells per 1 ton of product at a worldwide annual meat consumption of 340 million tons,[12] regenerative treatments demand 10^{9}–10^{10} cells per therapy and a batch production volume of 10^{12} cells to achieve large-scale economic and sustainable processes.[13,14]

S. B. Rauer, L. Stüwe, L. Steinbeck, G. Fischer, S. Wennemaring, J. Marschick, M. Wessling, J. Linkhorst
Chemical Process Engineering
RWTH Aachen University
Forckenbeckstr. 51, 52074 Aachen, Germany
E-mail: john.linkhorst@tu-darmstadt.de

S. B. Rauer, M. Wessling
DWI - Leibniz Institute for Interactive Materials
Forckenbeckstr. 50, 52074 Aachen, Germany

The ORCID identification number(s) for the author(s) of this article can be found under https://doi.org/10.1002/smll.202404183

DOI: 10.1002/smll.202404183

M. A. S. de Toledo, S. Koschmieder
Department of Hematology
Oncology, Hemostaseology, and Stem Cell Transplantation
Faculty of Medicine
RWTH Aachen University
52074 Aachen, Germany

M. A. S. de Toledo, S. Koschmieder
Center for Integrated Oncology Aachen Bonn Cologne Düsseldorf (CIO ABCD)
52074 Aachen, Germany

J. Linkhorst
Process Engineering of Electrochemical Systems
Department of Mechanical Engineering
Technical University of Darmstadt
Otto-Berndt-Str. 2, 64287 Darmstadt, Germany

These cell densities cannot be achieved by applying conventional planar cultivation systems, which display low surface-to-volume ratios, insufficient scalability, and lack the required control units for central process parameters.[2,15,16] Methods applied to achieve industrially relevant anchorage-dependent cell yields such as human embryonic kidney cells 293 (HEK293), Vero cells, satellite cells, or human pluripotent stem cells (hPSC) currently encompass readily scalable 3D cultivation systems based on the suspension of cellular aggregates or cell-containing microcarriers.[17–19] Although recent progress in aggregate cultivation could significantly boost its achievable cell densities,[20–22] current variations of this method only provide limited control over the homogeneity of the aggregate diameter leading to the formation of necrotic cores.[23,24] This limitation originates from oxygen and nutrient gradients developing in larger tissues and can be overcome by microcarrier-based approaches in which micrometer-sized beads (100–300 µm) provide the required surface area for cell attachment and proliferation to confluent monolayers.[25,26] In addition to the benefits regarding substrate and metabolite exchange, microcarriers provide high surface-to-volume ratios,[27] allow adequate control over aggregate formation by the dosage of fresh microcarriers,[28,29] and can be employed in various cultivation systems, such as fluidized bed, packed bed, and stirred tank bioreactors (STBR), making microcarriers the most promising candidate for maximizing cell yields.[30,31]

However, despite the potential and recent success of microcarriers in industrial-scale biomanufacturing, current cultivation is restricted to particle systems based on dextran, polystyrene, gelatin, and cellulose, which have limitations regarding their possible material and surface modifications.[2,31] Since properties such as topography, mechanical stiffness, or the presentation of biochemical ligands constitute critical influencing factors in terms of cell phenotype, differentiation potential, and genetic stability,[6] microcarrier systems enabling a greater degree of control over central particle characteristics could significantly improve the production of functional mammalian biomass. A distinct class of materials that holds great promise for applications requiring tailorable tissue-like properties are synthetic hydrogels. These 3D polymer networks structurally and physically resemble the extracellular matrix (ECM), featuring biocompatibility, porosity, softness, viscoelasticity, hydrophilicity, and super-absorbency while offering additional benefits such as physicochemical adaptability, stimuli-responsiveness, decreased batch-to-batch variability, and reduced immune response compared to xenogeneic or allogeneic materials.[32]

Within the category of hydrogels, poly(N-isopropylacrylamide) (PNIPAM), in particular, has attracted considerable attention for *in vitro* and *in vivo* applications due to its facile and flexible synthesis routes, low cytotoxicity, and its thermoresponsive nature.[33,34] Although recent advances have led to the fabrication of various functional PNIPAM-based particles,[35] fibers,[36] films,[37] and 3D macrogels,[38] applicable to drug delivery,[39] biosensing,[40] mechanical cell stimulation,[41] or enzyme-free cell harvest,[42] limited work has yet been performed on the transfer of these hydrogel technologies to industrial-relevant cultivation techniques. In this context, most of the corresponding studies focused on grafting PNIPAM on conventional microcarrier systems to equip them with the desired thermoresponsive behavior.[43–46] However, considering that the PNIPAM layer only accounts for a marginal fraction of the total microcarrier, the products of these grafting processes typically do not exhibit all of the beneficial structural and physicochemical hydrogel properties. Since PNIPAM also inherently lacks cell adhesion motifs, the achievable cell attachment efficiency relies moreover heavily on the layer thickness and grafting density, which makes precise process control vital to achieve sufficient cell-bead interaction.[47] A possible remedy for these grafting-related challenges is the fabrication of microcarriers solely from hydrogel-forming polymers by UV-polymerization. Using this approach, the inherent flaws of PNIPAM, including the lack of mechanical strength, the insufficient presence of bioactive ligands, and the limited loading capacity, are typically counteracted by the incorporation of functional co-monomers.[33,48] This principle was recently exploited to produce hydrogel microcarriers of PNIPAM-poly (ethylene glycol) diacrylate (PEGDA)—gelatin methacryloyl (GelMA) that could successfully support the expansion of human-derived glioma cells (U87) in microtiter plate and STBR cultivations.[47]

Here, we employ a droplet-microfluidic approach to leverage the synthetic co-monomer acrylic acid (AAc) in a UV-initiated reaction to expand the properties and functionality of PNIPAM hydrogels. This process results in the development of innovative ECM-mimicking microcarriers that exhibit the ability to locally present cytokines, facilitate cell expansion, and support macroscopic tissue formation. The use of AAc as a co-monomer is particularly advantageous for PNIPAM-based hydrogels in biomedical and biotechnological applications due to its ability to strengthen the gel network and introduce functional carboxyl (R-COOH) groups into the polymer matrix.[33] Similar to the natural ECM where glycosaminoglycans (GAG) and proteoglycans facilitate water retention and dictate the transport of bioactive ligands by electrostatic interactions,[49–51] AAc provides a synthetic way of generating hydration, compressive resistance, and structural integrity by binding large amounts of water.[52,53] The deprotonation of AAc at physiological pH introduces negative charges to the hydrogel that can interact with cations and positively charged protein sequences to control their transport, storage and release.[54] We harness these carboxyl groups to either electrostatically or covalently functionalize microcarriers with cell adhesive and cell fate-modulating motifs, which solves literature-reported challenges regarding the biocompatibility of PNIPAM-co-AAc hydrogels at elevated AAc concentrations.[37] In this context, our study investigates the novel idea of introducing a dual conjugation mechanism for volatile bioactive agents, including interleukin 3 (IL3) and vascular endothelial growth factor (VEGF), into soft hydrogel microcarriers facilitated by a single functional group. This approach shows potential in distinguishing between plasma membrane bound and internalized growth factors in terms of immobilization strategy, which could be harnessed to optimize their respective stability and bioactivity. By choosing a synthetic co-monomer, namely AAc, our system enables the controlled ECM-mimicking conjugation of arbitrary bioactive molecules and mixtures with a fully synthetic core hydrogel, which is difficult for bioactive core particles without simultaneously altering other microcarrier properties. The PNIPAM-co-AAc system therefore presents a versatile platform technology of highly adaptable hydrogel microcarriers that can potentially tackle the challenges

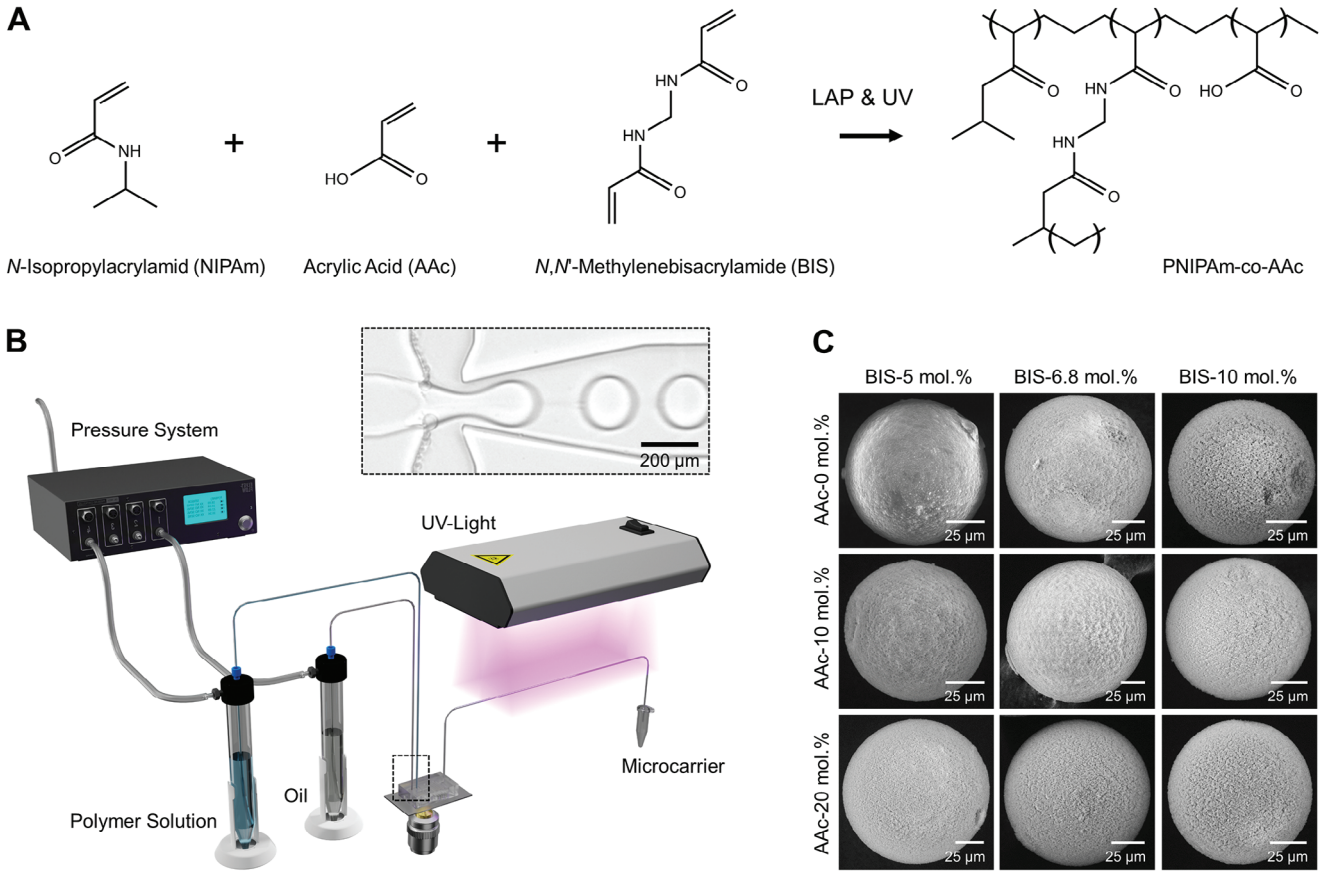

Figure 1. Overview of the microfluidic PNIPAM-co-AAc particle production applying a combination of cyto-compatible LAP photoinitiator and UV light. A) Chemical equation describing the formation of PNIPAM-co-AAc hydrogels via BIS crosslinking. B) Microfluidic setup for water-in-oil droplet generation and subsequent in-tube polymerization. C) Scanning electron microscopy images presenting the particle morphology in dependency of AAc co-monomer and BIS crosslinker content as molar fraction.

regarding the control and preservation of phenotypical attributes, cellular differentiation potential, and genetic stability by cell-type specific modifications, while also reducing the costs of valuable bioactive ligands by localized delivery. The provided correlation between simulated shear stress distribution, particle stability, and cell health increases the relevance of the study for industrial applications, such as lab-grown meat.

2. Results and Discussion

2.1. Chemistry, Fabrication, and Structural Microcarrier Properties

For the rapid generation of micrometer-sized PNIPAM-co-AAc particles, we combined a microfluidic droplet generator with a photo-initiated free radical chain polymerization based on lithium phenyl-2,4,6-trimethylbenzoylphosphinate (LAP) (**Figure** 1A). The corresponding microfluidic chip features a conventional T-junction layout displaying 200 µm wide inlet channels and a 400 µm wide outlet channel (Figure 1B). The system is capable of producing monodisperse water-in-oil (W/O) emulsions that are stabilized against droplet coagulation by supplementing the aqueous phase with 10 vol.% glycerol and 16.7 vol.% Pluronic F-68 at a production rate of 300 particles per minute with a polydispersity index (PDI) of 0.0034–0.0213 depending on the co-monomer content (Figure S1, Supporting Information). Since our initial studies revealed that long-chain alcohols such as 1-octanol are unsuitable for LAP-initiated photopolymerization of W/O droplets, likely due to the transition of reactants from the disperse to the continuous phase, the oil phase was adjusted to AR20 silicon oil. Figure 1C presents scanning electron microscopy (SEM) images of the resulting particles dried by solvent evaporation under vacuum for various combinations of AAc co-monomer and N,N-methylenbis-(acrylamide) (BIS) crosslinker contents. The particles display a dimensionally stable spherical shape of minor surface roughness, which originates from a nanometer-sized porosity that is more pronounced for increasing AAc and BIS contents. This observation contradicts the corresponding literature, where increases in AAc content usually lead to a decrease in pore size and elevated BIS concentrations typically result in smaller but more homogeneous pores.[55,56] Potential explanations for the reverse effects of the co-monomer and cross-linker content on particle morphology could be related to process parameters, including exposure time and intensity, differences in aqueous phase composition, such as the absence of stabilizing and thickening agents, or variations in the drying process, which is known to significantly influence morphological gel properties.[57,58] In fact, switching the

drying method of PNIPAM-co-AAc microcarriers from solvent evaporation to freeze drying can be actively used to transition the particle porosity from the nanometer to the micrometer scale (Figure S2, Supporting Information). Since the pore size dictates interactions between living cells and their substrates,[59] tuning gel porosity constitutes a valuable tool in generating application-specific structural particle features. Generally speaking, cells require a pore size in the order of their diameter to easily infiltrate their substrate,[60] while the nanometer-sized surface roughness substantially affects cell adhesion, growth, and maturation.[61] In terms of industrial-scale biomanufacturing, the presence of micrometer-sized pores in microcarriers can significantly increase the usable cultivation area and protect infiltrated cells from shear forces generated by the agitator. However, for processes that focus on the production of cell mass rather than biologicals, cell infiltration can negatively impact the final cell yield by entrapping cells within the microcarrier.

2.2. The Effect of Co-Monomer and Crosslinker Content on Global Gel Properties

2.2.1. Acrylic Acid Integration and Surface Charge

In addition to the influence of structural substrate characteristics, cellular behavior can additionally be dictated by the chemical composition of the hydrogel network, which directly influences its surface charge, wettability, mechanical properties, and stimuli-responsiveness. With respect to PNIPAM-co-AAc, these substrate characteristics are mainly controlled by the AAc co-monomer and BIS crosslinker content. **Figure** 2A and B present powder Fourier-transform infrared (FTIR) spectra of freeze-dried PNIPAM-co-AAc particles featuring 0 mol.% (A) and 20 mol.% (B) AAc. These spectra provide information on the overall gel composition and verify the successful incorporation of AAc by the presence of a COOH-specific peak at 1715 cm^{-1}, which is present for gels containing 20 mol.% AAc, and absent for pure PNIPAM hydrogels.[62] The relative peak height is similar to the corresponding literature investigating the composition of PNIPAM-co-AAc nanogels of varying AAc concentrations by FTIR.[63]

Since AAc exhibits a pKa value of 4.2[34], resulting in the deprotonation of the carboxyl groups at physiological pH, integration of AAc can also be monitored via zeta potential measurements. Figure 2C depicts the zeta potentials of PNIPAM-co-AAc particles for different molar AAc fractions at a pH of 7.4. While pure PNIPAM gels exhibit an approximately neutral surface charge featuring a zeta potential of -1.38 ± 0.28 mV, our data indicates a proportional relationship between co-monomer content and zeta potential, where an AAc increase from 10 mol.% to 20 mol.% leads to a decrease in zeta potential from -17.36 ± 1.52 to -26.54 ± 2.44 mV. These results demonstrate that both the functionalization degree and the surface charge are readily tunable via the AAc content during polymerization.

2.2.2. Mechanical Hydrogel Properties

The bulk mechanical hydrogel properties were determined by tensile tests on $20 \times 10 \times 1$ mm PNIPAM-co-AAc flat films polymerized in custom 3D-printed molds (Figure S3, Supporting Information). The polymerization conditions were adapted from the particle fabrication procedure to ensure comparability between hydrogel films and microcarriers. Because the hydrogels are intended as substrates for cell cultivation, the films were analyzed in the wet state to emulate cultivation conditions. Figure 2D shows the stress-strain curves of the flat films as a function of the AAc co-monomer and BIS crosslinker content measured at room temperature. Each stress-strain curve features two distinct regions of differing slopes located above and below 0.15 strain. These regions are an artifact of the clamping process, where film pre-wetting leads to hydrogel swelling and causes an initial loss in film tension. Consequently, we extracted the elastic (E)-moduli, which describe the stiffness or elasticity of a material, from the slope between 0.2 and 0.3 strain where preparative influences can be neglected.

The resulting values are presented in Figure 2E and reveal a linear correlation between crosslinker concentration and E-modulus. BIS contents between 5 and 10 mol.% lead to E-moduli spanning from 3.4 to 13.9 kPa. When comparing these values with the stiffness of natural tissues, the corresponding PNIPAM-co-AAc hydrogels are able to mimic the mechanical properties of the microenvironment of fibroblast (3 kPa), smooth muscle cell (5 kPa), skeletal muscle cell (12 kPa), and chondrocyte (14 kPa).[64] However, since BIS concentrations that lie below or exceed the investigated molar fractions are also feasible for gel polymerization, proximate tissue regions such as the softer microenvironment of neurons (< 1 kPa) or the stiffer surroundings of osteoblasts (20 kPa) can potentially be replicated. The E-moduli achievable with PNIPAM-co-AAc hydrogels are, therefore, significantly softer than conventional microcarriers such as Cytodex 1 (870 kPa),[65] or Cytodex 3 (50 kPa) and mimic the natural ECM more closely.[66] Since substrate elasticity influences lineage specification and should hence be matched to the cell type of interest, this ECM resemblance could prove crucial for currently anticipated *in vitro* technologies, such as stem cell expansion or the production of lineage-committed cells in STBR.[67] In contrast to the crosslinker content, the AAc concentration has only a negligible effect on the E-moduli. All data points measured at constant molar BIS and varying molar AAc content are located within the standard deviation, indicating insignificant alterations. The results of our tensile tests are supported by nanoindentation measurements of spherical microparticles using an Optics11Life Pavone system. Since the bulk moduli did not significantly vary with the AAc content of the hydrogels, the corresponding study solely focused on determining the local elasticity depending on the BIS crosslinker content. The resulting stiffness values and one exemplary measurement sequence per particle type are presented in Figure S4, Supporting Information, where 5 mol.% BIS leads to an effective Young's modulus of 0.3 ± 0.1 kPa, 6.8 mol.% BIS to 3.1 ± 2.0 kPa, and 10 mol.% BIS to 6.8 ± 6.5 kPa.

Figure 2F presents the fracture points of PNIPAM-co-AAc hydrogel films, which, as predicted by literature,[33] indicate the strengthening of the polymer network by the introduction of both, increasing amounts of AAc and crosslinker. While elevating the BIS concentration leads to significant increases in fracture stress accompanied by a reduction in fracture strain, increasing the molar AAc fraction enhances both values simultaneously, reflecting the mechanical benefits of AAc co-polymerization.

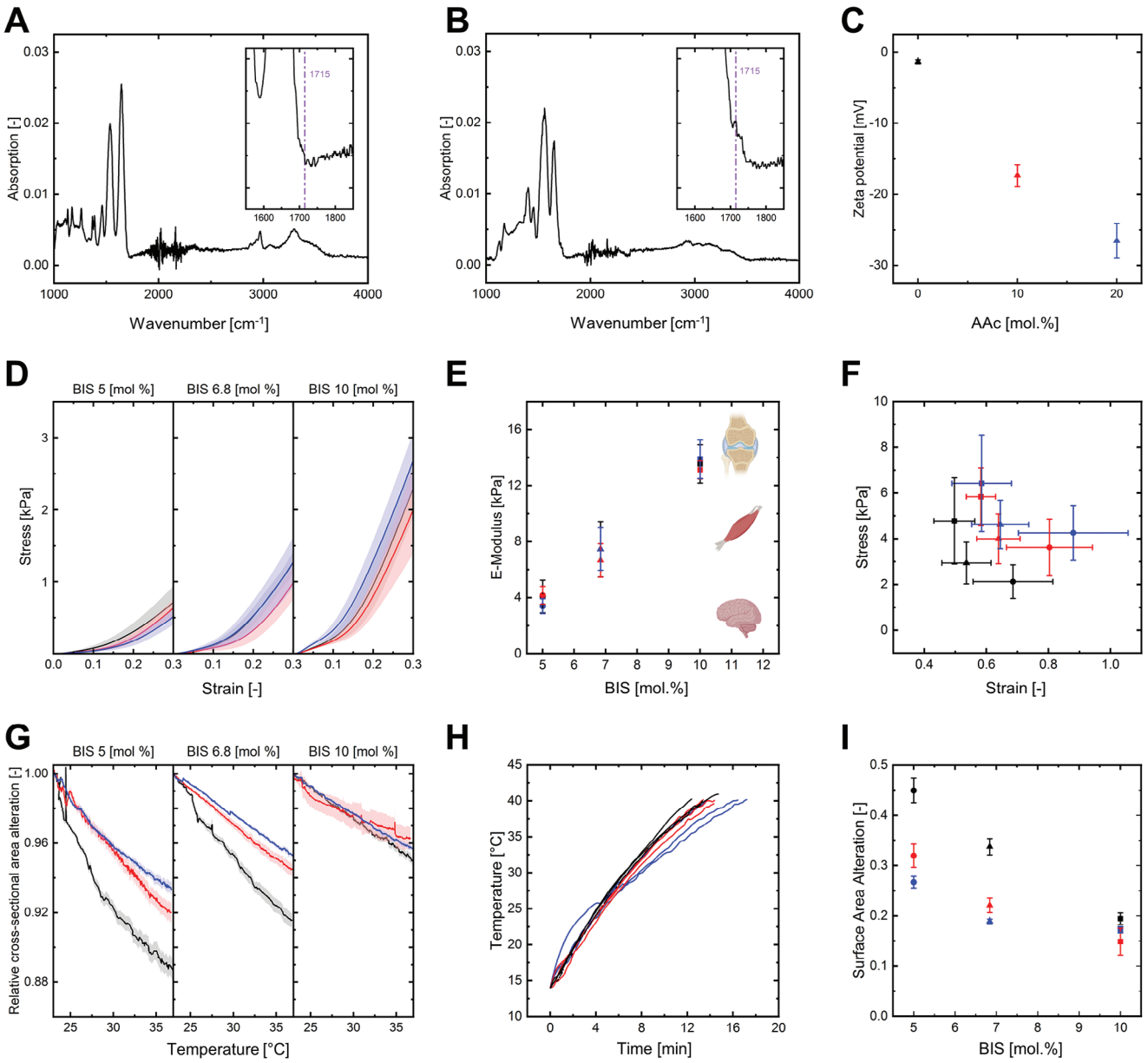

Figure 2. Material properties of PNIPAM-co-AAc hydrogels produced by UV-initiated radical polymerization in dependency of the AAc co-monomer and BIS crosslinker content; color code: **0 mol.% AAc**, **10 mol.% AAc**, **20 mol.% AAc**; symbols: ● = 5 mol.% BIS, ▲ = 6.8 mol.% BIS, ■ = 10 mol.% BIS. A) Powder FTIR spectrum of freeze-dried PNIPAM particles. B) Powder FTIR spectrum of freeze-dried PNIPAM-co-AAc particles featuring 20 mol.% AAc co-monomer content. C) Overview of the particle surface charge expressed in terms of zeta potential at a pH of 7.4. D) Stress-strain diagrams of UV-polymerized PNIPAM-co-AAc flat films recorded via tensile testing at a stretching speed of 0.2 mm/s presented as average and standard deviation. E) Elastic modulus of PNIPAM-co-AAc flat films determined between 0.2 and 0.3 strain. E-moduli of natural micro-environments: neuronal ≈ 1 kPa, fibroblast ≈ 3 kPa, smooth muscle cell ≈ 5 kPa, skeletal muscle cell ≈ 12 kPa, chondrocyte ≈ 14 kPa, osteoblast ≈ 20 kPa. F) Fracture stress and strain of PNIPAM-co-AAc flat films. G) Progression of temperature-induced particle volume change expressed in relative cross-sectional particle area. H) Time-dependent temperature profiles applied for initiating a particle phase transition. I) Total change in particle surface area resulting from a temperature-induced phase transition. N = 10.

2.2.3. Temperature-Induced Volume Phase Transition

The volume phase transition of PNIPAM-co-AAc hydrogel particles was evaluated in dependence of the AAc co-monomer and BIS crosslinker content by exposing particles submerged in deionized (DI) water to temperature ramps of 25 °C to 40 °C. The temperature-dependent hydrogel response was recorded using a bright-field microscope, and the progression of the volume phase transition was visualized in terms of the relative cross-sectional area, which is presented in Figure 2G. The resulting graphs show the specific volumetric collapse of PNIPAM at elevated temperatures, which is due to the transition from an extended random

coil to a glob conformation upon surpassing the lower critical solution temperature (LCST).[68] Below the LCST, the amide groups of PNIPAM readily interact with water molecules via hydrogen bonding, stabilizing the extended polymer structure and swelling the hydrogel matrix. However, as the temperature increases above the LCST, the increasing entropy of the water molecules intensifies the interaction between the hydrophobic isopropyl groups, leading to the collapse of the polymer network under the expulsion of water (syneresis).[69]

In contrast to the archetypal sigmoidal volume phase transition of PNIPAM reported in the literature,[70] our results demonstrate gel responses that resemble exponential decay for 5 mol.% BIS, while gels with higher BIS content collapse more linearly. In this context, the hydrogel dimensions and the slope of the temperature profiles are likely to play a central role. Increasing the size of a hydrogel decelerates its temperature-dependent syneresis, where the characteristic swelling and shrinking time is proportional to the hydrogel dimensions.[68] Combining the effect of gel size with a continuous temperature ramp as applied in our experiments (Figure 2H) could therefore lead to inertial effects, where the hydrogel response lags behind the temperature. Other known factors that might impact the dynamic progression, temperature, and extent of the volume phase transition are co-polymerization, co-solvents, and adsorptive events.[71–73] However, since the profiles of the relative cross-sectional area are similar for identical AAc contents, deviations from an ideal sigmoidal progression could only originate from the influence of additive residues (glycerol, pluronic F-68), which may be entrapped within the gel network during polymerization.

Figure 2I presents the change in total surface area of a hydrogel particle upon completing a temperature ramp from 25 °C to 40 °C. The data is calculated from the relative cross-section area and reveals that increases in both AAc and BIS content weaken the hydrogel's temperature response. While a higher crosslinking density generated by an elevated BIS concentration restricts the gel swelling capacity by decreasing the matrix mesh size and lowering the polymer chain mobility,[33,74] increasing the AAc fraction leads to enhanced water retention above the LCST. The hydrophilic carboxyl groups introduced by co-polymerization strengthen the hydrogen bonds and hamper the hydrogel's collapse by creating repulsive electrostatic forces due to their deprotonation at neutral pH.[55,75,76] The improved interaction between water molecules and AAc-containing hydrogels is typically accompanied by a significant increase in LCST since more thermal energy is required to disrupt existing hydrogen bonds.[77,78] For cell cultivation, the improved gel hydration related to AAc is a desired property that preserves the hydrogel's pore network and maintains permeability for essential compounds, including nutrients, metabolites, and gases, even above the LCST.[53] The dependency of the syneresis on the AAc co-monomer and BIS crosslinker content, moreover, provides the opportunity to tailor the extent of the volume phase transition, where a less pronounced temperature response could provide benefits for mechanical cell actuation, while increased responses might be applied to facilitate enzyme-free cell harvest. A summary of the PNIPAM-co-AAc hydrogel properties is provided as table of explicit values in Figure S5, Supporting Information.

2.3. Hydrogel Functionalization via Acrylic Acid

Since adherent cells attach to their ECM via specific receptor-ligand interactions, synthetic hydrogels, which naturally lack adhesive moieties, typically require additional functionalization to facilitate appropriate cell attachment. For PNIPAM-co-AAc, a convenient reaction route is the covalent bonding of adhesive ligands to the carboxyl group of AAc via the well-established 1-ethyl-3-(3-dimethylaminopropyl)carbodiimide hydrochloride (EDC) - N-Hydroxysuccinimide (NHS) coupling reaction. EDC is a zero-length crosslinker that reacts with a carboxyl group to form a reactive but unstable O-acylisourea intermediate in an initial activation reaction. O-acylisourea can react rapidly with compounds that present amino groups ($R\text{-}NH_2$) under the formation of amide bonds and the release of isourea by-products. However, since the activated carboxyl group readily hydrolyzes in aqueous reaction solutions and therefore has short half-lives of the order of seconds,[79] the O-acylisourea intermediate requires stabilization to achieve the proper reaction efficiencies. The necessary increase in intermediate stability is typically facilitated by the addition of NHS, which reacts with the unstable O-acylisourea to form a semi-stable NHS ester. The NHS ester features an improved half-life in the order of hours and is highly reactive toward amine-containing reactants such as adhesive proteins or cell fate-modulating cytokines and growth factors.[80] A scheme of the EDC-NHS coupling reaction is presented in **Figure 3A**.

For verifying whether EDC-NHS coupling is suitable for hydrogel functionalization, we investigated the covalent bonding of the NH_2-containing model molecule Lucifer yellow (LY) to PNIPAM-co-AAc particles, which is schematically depicted in Figure 3B. LY is a fluorescent molecule that is excitable at 428 nm and emits light around 536 nm. In addition, the molecule features a negative charge due to the presence of two sulfonic acid groups, which results in repulsive electrostatic interactions with AAc and hence prevents false positives due to adsorption. Figure 3C shows confocal fluorescence microscopy images of PNIPAM-co-AAc hydrogel beads functionalized with 100 µM LY at pH 5 and compares them with a control sample of 10 mol.% AAc. The control sample was exposed to LY in the absence of EDC-NHS at identical reaction conditions and demonstrates their adsorptive interaction. Therefore, the presence of a fluorescence signal in samples functionalized by EDC-NHS crosslinking proves that amine-containing compounds can be covalently coupled to the hydrogel matrix, while the absence of a fluorescent signal in the control sample rules out LY adsorption. The images display a restriction of the fluorescent signal to the particle shell, which might either indicate a limited transport of reactants into the hydrogel matrix or the loss of emission intensity due to the opaque nature of the hydrogel. Contrary to AAc-containing control samples, pure PNIPAM beads exhibit an attractive adsorptive interaction with LY, most likely due to the missing electrostatic repulsion (Figure S6, Supporting Information).

2.4. Microtiter-Plate Cultivation on Fibronectin-Functionalized PNIPAM-co-AAc Microcarrier

Considering that already marginal AAc co-monomer concentrations exceeding 4 mol.% can induce cytotoxic gel behavior,[37,81,82]

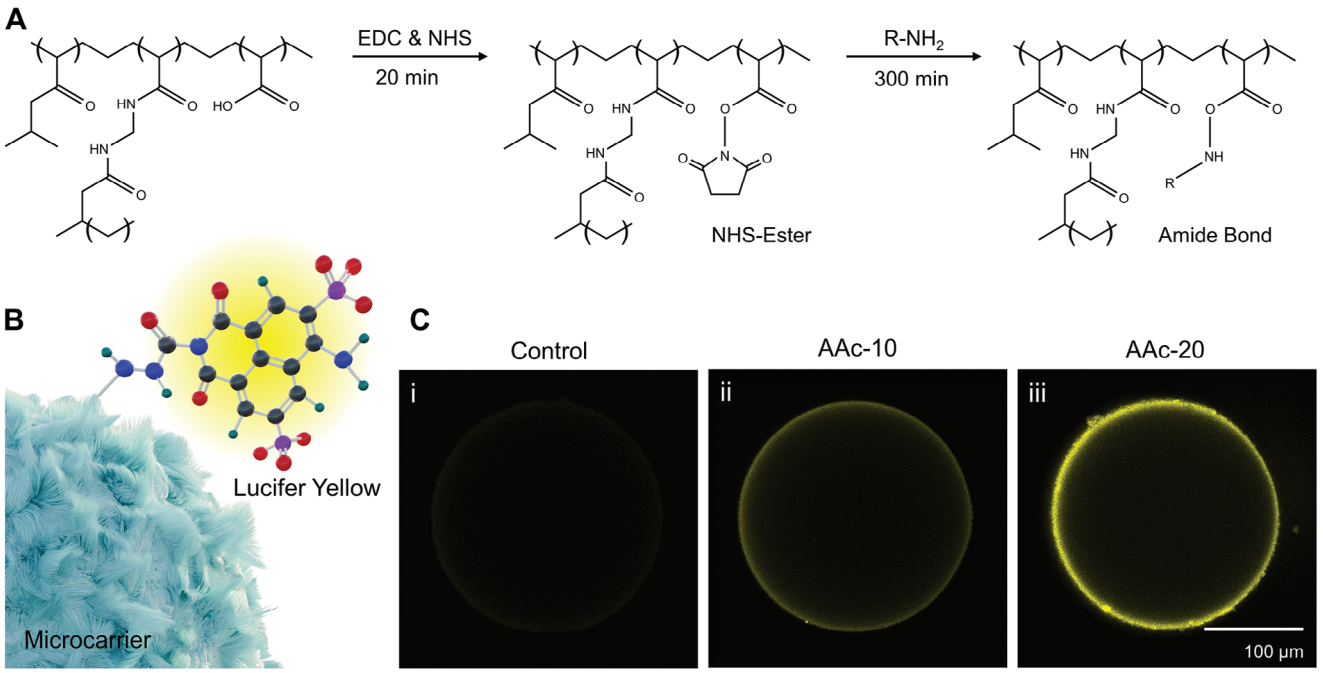

Figure 3. Functionalization of PNIPAM-co-AAc hydrogels via EDC-NHS coupling. A) Reaction progression comprising the activation of the carboxyl groups by an EDC-NHS priming step followed by the covalent coupling of an amine-presenting compound to the reactive NHS-ester. B) Schematic illustration of the model reaction applied to verify the success of EDC-NHS coupling to PNIPAM-co-AAc particles. C) Confocal fluorescence microscopy images of PNIPAM-co-AAc particles: i) Adsorptive control depicting the interaction between LY and PNIPAM-co-AAc particles in the absence of EDC-NHS. ii) Covalent EDC-NHS coupling of LY to a PNIPAM-co-AAc particle featuring 10 mol.% AAc. iii) Covalent EDC-NHS coupling of LY to a PNIPAM-co-AAc particle featuring 20 mol.% AAc.

the primary focus of our microtiter plate experiments was investigating the interaction between the degree of AAc labeling and cell proliferation. As an acid featuring a pKa of 4.2, AAc releases significant amounts of hydrogen ions into the medium, reducing the pH to non-physiological levels. This acidification can disrupt the pH homeostasis, alter enzyme activity, and damage lipids, proteins, and DNA.[83,84] Since deprotonation simultaneously causes an increase in negative surface charge, elevated AAc concentrations also hamper cell attachment by generating repulsive electrostatic interactions between hydrogels and cells, which generally have a negative membrane potential.[85] While medium acidification can be prevented by removing hydrogen ions prior to inoculation by appropriate washing protocols, challenges related to the surface charge of AAc-containing hydrogels can be minimized by the functionalization of the carboxyl groups with cell adhesive molecules.

Figure 4A shows the results of static microtiter-plate cultivations of L929 mouse fibroblast cells labeled with CellMask Orange (red) on fibronectin (FN)-functionalized PNIPAM-co-AAc beads of varying AAc co-monomer content. L929 cells appear adherent after 1 day of cultivation and proliferate readily into dense cellular monolayers over 7 days, interconnecting microcarriers to mm-sized tissues independent of the AAc-content (Figure S7, Supporting Information). The images present our best coupling results in terms of cell attachment and growth, which were achieved by EDC-NHS coupling in an aqueous 50 mM MES-buffer solution containing 300 g mL^{-1} FN solution at pH 5 and were verified by FTIR spectroscopy (Figure S8, Supporting Information). Comparison to the corresponding literature indicates that our reaction conditions are presumably close to the optimum range for FN coupling. Generally speaking, decreasing the reaction pH improves NHS-ester stability but reduces the reactivity of amine-containing ligands by increasing their protonation degree.[86] Therefore, in theory, acidic environments benefit the activation reaction, while pH values above the isoelectric point (iP) of the protein are favorable for ligand coupling. However, this fundamental relationship between intermediate stability and ligand reactivity is additionally overlapped by charge interactions, where attractive electrostatic forces between hydrogel and ligands can significantly improve the coupling efficiency by molecular recruitment, even in cases where the reaction pH undercuts the iP of the protein. This phenomenon was demonstrated for EDC-NHS coupling of bovine serum albumin (BSA) to AAc, in which reaction pH values located in between the pKa of AAc and the iP of BSA resulted in improved protein binding.[87] Considering that FN exhibits an iP of 5.5–6.0,[88] and AAc features a pKa of 4.2, choosing a reaction pH of 5 results in slight attractive electrostatic interaction between negatively charged AAc and positively charged FN, without over-protonating the amino-groups of the ligand. However, since salt ions can shield the resulting charges, the advantageous recruitment effect originating from an ideal reaction pH can easily be negated by excessive buffer concentrations. This adverse effect of elevated salt levels becomes visible as hampered cell proliferation on PNIPAM-co-AAc microcarriers functionalized at identical reaction conditions but a 10 times higher buffer concentration of 500 mM (Figure S9, Supporting Information). The successful cell expansion on FN-functionalized microcarriers sharply contrasts with

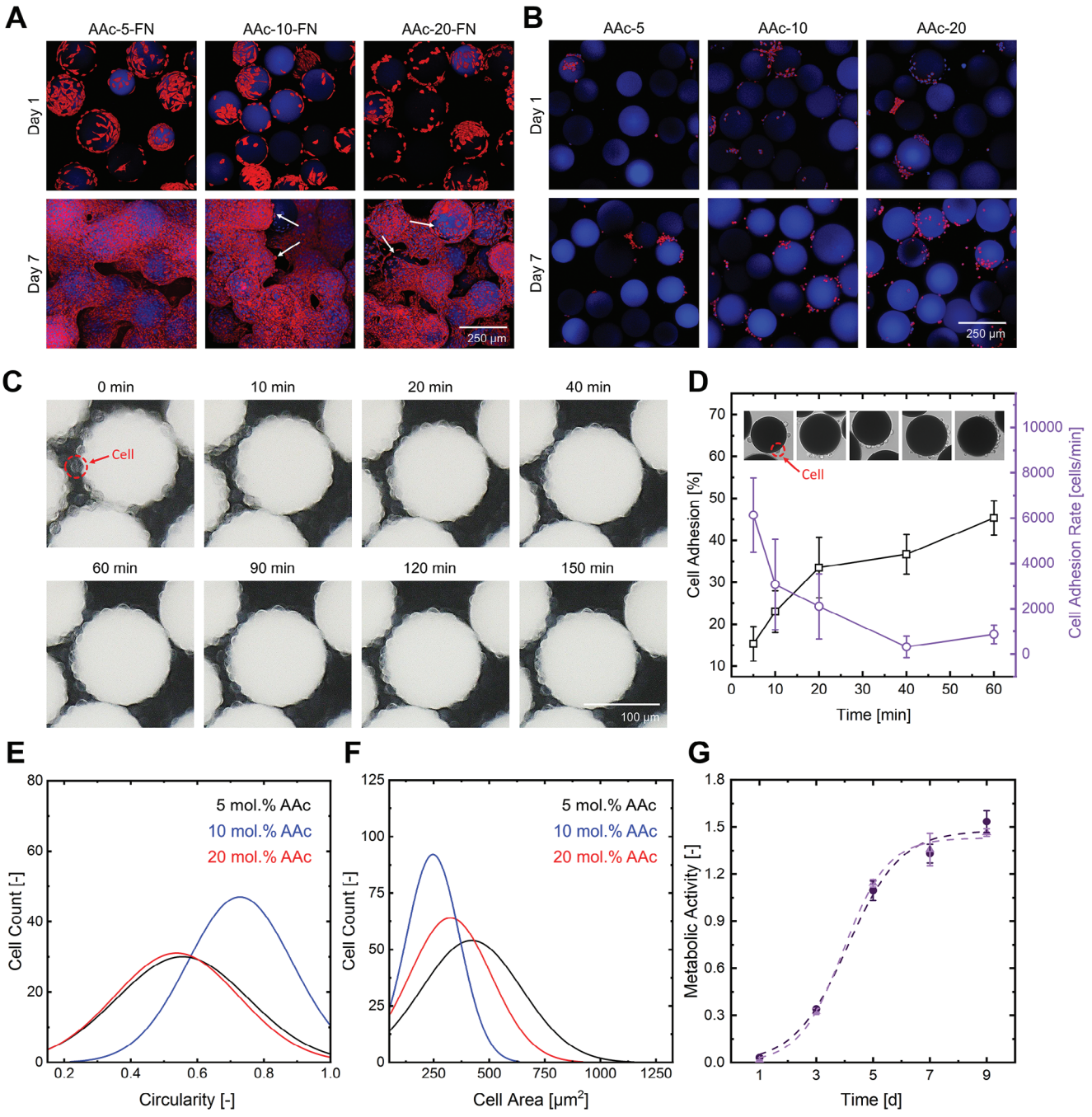

Figure 4. Static microtiter plate cultivation of L929 mouse fibroblast cells on PNIPAM-co-AAc microcarriers of 10 mol.% BIS content and various AAc labeling degrees. A) Confocal fluorescence microscopy images presenting the cell proliferation on FN-functionalized microcarriers; arrows indicate areas of weak cell-substrate interactions. B) Confocal fluorescence microscopy images presenting the cell proliferation on non-functionalized microcarriers (control). C) Time lapse microscopy series showing cell adhesion on the upper hemisphere of FN-functionalized PNIPAM-co-AAc microcarriers of 5 mol.% AAc. An exemplary cell located on the surface of a microcarrier is indicated by a dotted red circle. D) Cell adhesion rate and time dependent cell adhesion expressed as percentage of the total number of seeded cells. An exemplary cell located on the surface of a microcarrier is indicated by a dotted red circle. E) Cell circularity distribution determined from day 1 cultivation images via ImageJ; N = 220. F) Cell spreading area distribution determined from day 1 cultivation images via ImageJ; N = 220. G) Relative cell growth acquired via a tetrazolium-based XTT cell proliferation assay conducted with cells cultivated in pure (▲) and leached (●) medium. Inoculation concentrations in relation to the microtiter plate area: $c_{A,B}$ = 200 000 cells cm^{-2}; $c_{C,D}$ = 200.000 cells per reaction tube; c_G = 5000 cells cm^{-2}.

the cell behavior on the corresponding control samples presented in Figure 4B. The results demonstrate that non-functionalized particles can neither support cell adhesion nor cell growth and hence prove the functionality and necessity of covalent adhesive coupling for cell cultivation.

Besides our initial study, which primarily investigates the expansion phase of the cultivation cycle, we also performed live-time experiments to generate data describing the initial stages of cell adhesion. Figure 4C presents a time-lapse microscopy series recorded with a Keyence VHX digital microscope, which enables recording and illumination of the upper microcarrier hemisphere on which cells sediment after seeding. The images show that most of the adhesion process happens within the initial 20 min after inoculation. In the interval between 20 and 40 min, cells subsequently undergo marginal migration events, before all visible cells finally reach their resting position as observable in Video S10 (Supporting Information). These results indicate that all cells contacting the microcarriers also adhere, which renders the adhesion efficiency for protein-functionalized PNIPAM-co-AAc microcarriers primarily dependent on the ratio between the projected particle area and the base area of the cultivation vessel. Figure 4D quantifies these observations as time dependent progression of the number of adherent cells normalized by the total number of seeded cells and uses them to determine time interval-specific adhesion rates. The cell adhesion process starts with a rate of 6100 adhering cells per min between 0 and 5 min. This rate subsequently drastically drops to 2100 adhering cells per min in the interval between 10 and 20 min, before finally ending at a rate of 870 cells per min measured in the time interval between 40 and 60 min. The saturation of the adhesion curve at approximately 50% is most likely due to cell accumulation at the border of the particle sediment originating from the significantly faster sedimentation speed of PNIPAM-co-AAc particles compared to L929 cells, which causes an excess of cells compared to the provided surface area. This effect is verified by the brightfield microscopy images attached to Figure 4D, which show a tightly packed cell layer restricted to one hemisphere for samples exceeding the 20 min time interval, and can be circumvented in STBR by intermittent stirring during the attachment phase.

In addition to these general observations regarding cell attachment and proliferation, conducting a more in-depth analysis of cell morphology can provide additional insight into the interactions between cells and their substrate. The attachment of adherent cells to their microenvironment is primarily mediated by integrin receptors that connect the intracellular actin cytoskeleton to extracellular ECM molecules via focal adhesions. The resulting supramolecular protein complexes are reinforced and stabilized by actin-myosin contractions, which generate tension and cause cell spreading on corresponding surfaces.[89] During this process, cells transition from a rounded morphology to a flattened one and increase their contact area significantly. Previous studies could reveal a proportional relationship between cell area and mean traction, rendering cell spread a valuable indicator for adhesion strength.[90,91]

Figure 4E presents the circularity of L929 mouse fibroblast cells plotted against the AAc-labeling degree. The data was extracted from images of cultivation day 1 and transfers morphological information into mathematical values, where a circularity of 1 represents a perfect circle, while a circularity of 0 describes a line. The graph shows that the distributions for cells expanded on microcarriers containing 5 and 10 mol.% AAc almost coincides, suggesting a similar cell-particle interaction for both labeling degrees. The respective mean values of 0.55 and 0.53 reveal a non-spherical cell shape and indicate anisotropic cell spreading on corresponding hydrogel beads. In contrast to the matching results obtained from samples of lesser co-polymerization degree, the normal distribution for particles containing 20 mol.% AAc is shifted to higher circularity values. This increase in cell roundness can either be interpreted as more isotropic cell spreading or weakened cell-hydrogel interaction. The uncertainty regarding the cause of these morphological changes can be clarified by investigating the cell spreading area, which is depicted in Figure 4F. The graphs demonstrate a substantial cell area decrease with increasing AAc fraction featuring mean values of 425 μm^2 for 5 mol.% AAc, 325 μm^2 for 10 mol.% AAc, and 250 μm^2 for 20 mol.% AAc. Considering that the contact area correlates with the mean cellular traction, our data hints at a significant reduction in cell adhesion strength at elevated co-polymerization degrees. This conclusion is highly coherent with effects observable in our fluorescence microscopy images of cultivation day 7 (Figure 4A), where an increase in AAc-labeling causes the formation of cell layer defects, which are exemplified by white arrows. Since mammalian cells exhibit a negative membrane potential, we hypothesize that the reduction in cell adhesion strength stems from increasing repulsive electrostatic interactions at elevated co-monomer contents. Assuming that a certain percentage of the functional groups will fail to react with FN, which is highly probable due to the progressive hydrolysis of the NHS ester during the coupling reaction, particles featuring a higher AAc content not only exhibit a higher degree of functionalization but also a higher negative surface charge due to the deprotonation of residual AAc. Finally, considering that our SEM and tensile test results revealed a negligible influence of the co-polymerization degree on structural and mechanical particle properties, a significant contribution of the surface topology and E-modulus to reducing cell adhesion can be excluded.

Although our microtiter-plate cultivations could successfully demonstrate that PNIPAM-co-AAc hydrogels support cell proliferation up to 20 mol.% AAc, potential cytotoxic effects related to diffusive release of unreacted educts cannot be unambiguously excluded from the corresponding results. Since our reaction system comprises several cytotoxic reactants, including glycerol, AAc, and N-Isopropylacrylamid (NIPAM), which can leach from the hydrogel matrix after polymerization and negatively impact cell viability and division rate,[92–94] we performed a tetrazolium salt-based cytotoxicity (XTT) assay comparing cell growth in the leached medium to cell growth in the pure medium. The respective growth curves are depicted in Figure 4G and prove in combination with our 7-day cell proliferation results (Figure 4A) the biocompatible nature of PNIPAM-co-AAc microcarriers purified according to our washing protocol. With less than 5% deviation in the absorption values, the XTT results indicate that the polymerized hydrogel components are non-cytotoxic and unreacted educts are successfully removed during purification.

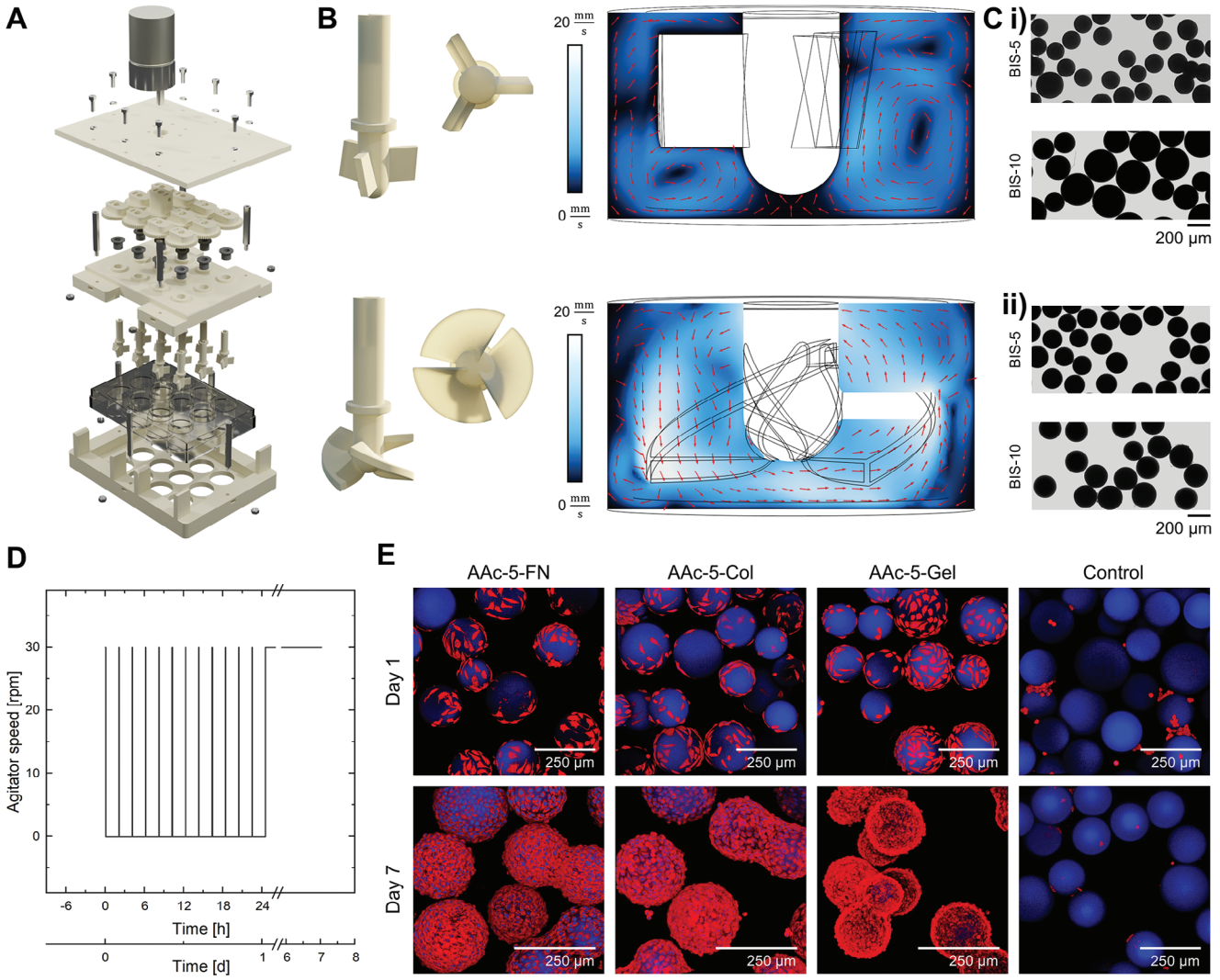

Figure 5. STBR setup, optimization, and L929 mouse fibroblast expansion on protein-functionalized PNIPAM-co-AAc microcarriers featuring 5 mol.% AAc co-monomer and 10 mol.% BIS content. A) Explosion drawing of the miniaturized STBR setup applied for suspended cell expansion adopted from Romero-Morales et al.[95]. B) Optimization of the agitator geometry regarding hydrodynamic dead zone formation at 30 RPM. 3D rendering of the oblique blade stirrer (top, left) and the propeller-type stirrer (bottom, left). Fluid dynamic simulation using Comsol Multiphysics for the oblique blade and propeller-type stirrer within the single-well dimensions of a 12 well microtiter plate (right). Dark blue zones indicate hydrodynamic dead zones. C) Verification of mechanical and structural microcarrier stability against particle-particle, particle-stirrer, and particle-wall contact as well as agitator-induced shear stress for soft (5 mol.%) and stiffer (10 mol.%) BIS crosslinked particles. The brightfield microscopy images demonstrate the absence of microcarrier damage or debris after 3 days of stirring at 70 RPM with the i) oblique blade stirrer and ii) propeller-type stirrer. D) Agitator sequence for cell expansion: 1 day of intermittent stirring alternating between 1 min of 30 RPM and 2 h of 0 RPM for homogeneous cell seeding; 6 days of continuous cell expansion at 30 RPM. E) Confocal fluorescence microscopy images presenting the cell proliferation on PNIPAM-co-AAc microcarriers featuring differing adhesive proteins and a non-functionalized control sample. Inoculation concentration in relation to the microtiter plate area: c = 200 000 cells cm^{-2}.

2.5. Stirred-Tank Bioreactor Cultivations

Since microcarriers are typically combined with STBRs to maximize cell yields, we investigated the expansion of L929 cells on suspended protein-functionalized PNIPAM-co-AAc beads to verify their applicability for industrial-scale biomanufacturing. The corresponding cultivations were conducted in a miniaturized bioreactor system, which is depicted in **Figure** 5A and enables 12 parallel suspension cultures in commercially available microtiter plates via gear transmission driven by a single electric motor. The device was adopted from Romero-Morales et al.'s Spinoo system and was slightly modified to better suit our experiments.[95] In this context, particularly our adjustments regarding the printing method and stirrer geometry are noteworthy as they simplify the manufacturing process and improve mixing significantly.

In the original Spinoo system, all bioreactor components exposed to medium require Parylene C deposition to inhibit medium adsorption within the porous structure of the components, which poses a potential contamination risk. Since component porosity directly results from applying fused deposition modeling (FDM), we switched to stereolithography

(SLA)-based printing, which produces nonporous structures without the need for additional coating steps (Figure S11, Supporting Information). Similar to the ULTEM1010 resin from Stratasys used for the original Spin∞ system, the high temp resin from formlabs applied for SLA is heat resistant up to a temperature of 238 °C in the absence of mechanical tension and, therefore, can be steam sterilized at 121 °C. In addition to replacing the printing method, the stirrer design required additional constructive adjustments since the original oblique blade geometry could not maintain microcarriers in suspension. This observation was verified in Comsol Multiphysics simulations, which demonstrate the formation of a hydrodynamic dead zone directly below the agitator shaft where microcarriers readily collect to form larger aggregates. This sedimentation issue could be solved by designing a propeller-type stirrer featuring blades that extend to the tip of the agitator shaft. The two types of stirrers and the respective fluid dynamic simulations are depicted in Figure 5B and prove the removal of the hydrodynamic dead zone by changing the agitator geometry. Figure 5C presents microcarriers of different crosslinking degrees which were exposed to an agitator speed of 70 RPM for 3 days in reactors equipped with both oblique blade and propeller-type stirrers, respectively. The brightfield microscopy images verify the stability of PNIPAM-co-AAc microcarriers independent of the hydrogel stiffness up to shear stress values of 1.2 Pa, generated at the tip of the propeller-type stirrer. An overview of the shear stress distribution within a compartment of the miniaturized STBR in dependency of the stirrer geometry and agitator speed is provided in Figure S12 (Supporting Information).

For the expansion of L929 cells in the miniaturized STBR system, a custom stirring sequence was applied according to Figure 5D. The sequence consists of two distinct stages, where the initial 24 h of intermittent stirring ensures homogeneous cell seeding and a complete particle volume phase transition, while the subsequent application of a constant agitator speed guarantees appropriate microcarrier suspension during cell cultivation. The success of our procedure is depicted in Figure 5E for 5 mol.% AAc-containing microcarriers covalently functionalized with various adhesive proteins, including FN, collagen (Col), and gelatin (Gel). The fluorescence microscopy images verify that cells are homogeneously distributed due to the initial seeding stage and readily adhere to all types of functionalized microcarriers after 1 day of cultivation. During the following 6 days at 30 RPM, single cells proliferate to dense cellular monolayers that can withstand a tip shear stress of 0.4 Pa on samples featuring adhesive moieties, while the non-functionalized control samples are not able to support cell expansion. In contrast to our static cultivations in microtiter plates, where particles and cells readily formed coherent clusters, in STBR cultivations, microcarriers are present as individual particles even at high confluency levels, indicating a sufficient bead suspension at relatively low agitator speeds. Concerning the different protein functionalizations, the results further demonstrate similar spreading and proliferation behavior on FN, Col, and Gel-functionalized microcarriers, which emphasizes the flexibility of EDC-NHS coupling with respect to potential reaction partners and generates the opportunity to tailor the surface chemistry toward specific cellular needs.

2.6. Growth Factor Functionalization

Growth factors (GF) are essential messenger molecules that regulate central cellular functions such as cell proliferation, apoptosis, migration, and differentiation by triggering intracellular signaling cascades upon binding to cell surface receptors.[96] Depending on their type, the resulting GF-receptor complexes can either indirectly cause a cellular response by transmembrane signaling or directly trigger an intracellular event by endocytic internalization. *In vivo*, the binding process of GF to receptors is mediated primarily by the ECM, which functions as a reservoir unit that stores and protects GF by sequestration, modulates their activity and organizes them on the cell surface.[97] Once sequestered, GF can be locally released by enzymatic cleavage and bind to the corresponding receptors as bioactive solutes or directly interact with surrounding cells in the ECM-bound state.[98]

Similarly to their necessity *in vivo*, GF also play a vital role in biotechnological processes, in which they constitute high-value supplements that ensure optimal cell viability, proliferation, functionality, and potency. However, contrary to their natural environment, where they are locally presented and controlled by the ECM, *in vitro* cultivations typically provide GF as medium-dissolved additives. This global supply as a solute significantly increases the process costs, since the required amount of cell-type-specific GF has to be achieved as the bulk phase concentration. In the context of microcarrier-based cultivations, a potential remedy to alleviate these expenses is the immobilization of GF within the bead matrix. This approach aims to focus GF presentation on the cell-proximate volume fraction of the bioreactor, drastically reducing the excess amount dissolved within the bulk phase. Furthermore, studies could demonstrate that GF-matrix conjugation can protect GF from degradation, which maintains their bioactivity over long periods of time, reduces the need for constant replenishment, and opens the possibility for microcarrier reuse.[99]

Considering the two previously discussed GF subcategories, which encompass internalized and non-internalized GF, a potential microcarrier platform technology should ideally facilitate both reversible and irreversible GF conjugation. While this multifunctionality could be realized solely based on the covalent immobilization of GF within the microcarrier, the release of such GF would either require additional cost-increasing medium supplements, such as enzymes, or a biodegradable matrix that significantly limits particle reusability. Therefore, we aimed to simultaneously integrate two distinct mechanisms of GF conjugation into a single non-degradable hydrogel type. Because our PNIPAM-based hydrogels are synthesized by co-polymerization with AAc, the most straightforward approach is to exploit the corresponding functional groups. While covalent GF binding can be facilitated by EDC-NHS-coupling similar to the previously presented adhesive modifications, a load-and-release behavior can be realized by electrostatic GF-matrix interactions generated by the deprotonation of the carboxyl group at physiological pH.

The functionalization of PNIPAM-co-AAc microcarriers with GF was investigated by analyzing the growth of empty vector (EV) transfected 32D cells in the vicinity of functionalized and non-functionalized microcarriers in microtiter-plate experiments. These murine myeloblast-like cells rely on interleukin-3 (IL3) signaling through the IL3 receptor (IL3R) and downstream

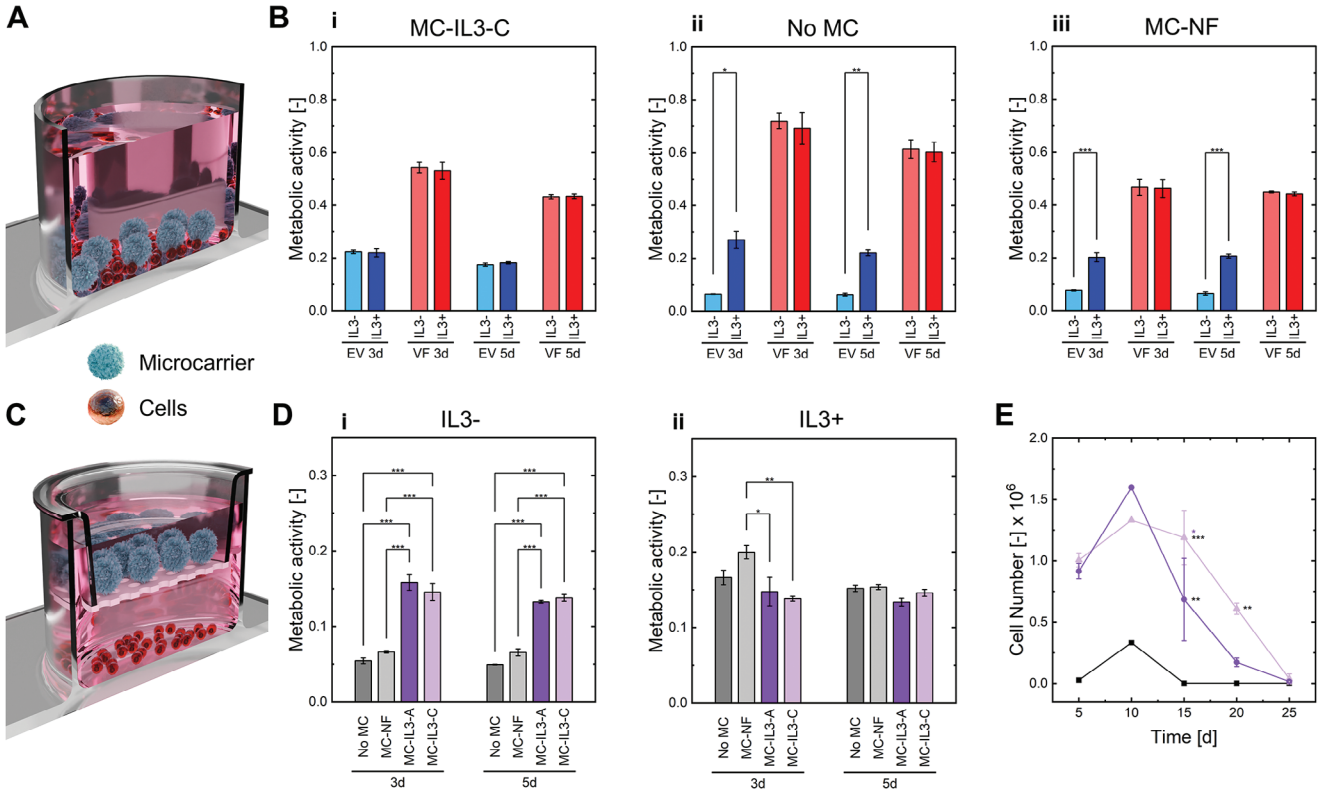

Figure 6. Impact of GF functionalization on EV and JAK2 VF transfected 32D myeloblast-like cells in microcarrier-based microtiter-plate cultivations. A) Principle of direct contact cultivation. B) Metabolic activity in IL3- and IL3+ supplemented medium in direct contact cultivations; B.i) in the presence of microcarriers covalently functionalized with IL3 (MC-IL3-C); B.ii) in the absence of microcarriers (No MC); B.iii) in the presence of non-functionalized microcarriers (MC-NF). C) Principle of transwell cultivation. D) Metabolic activity for No MC, MC-NF, adsorptively-functionalized microcarrier (MC-IL3-A), and MC-IL3-C in transwell cultivations; D.i) in IL3- media; D.ii) in IL3+ media. E) Comparison of non-functionalized (■), adsorptively-functionalized (●), and covalently-functionalized (▲) microcarriers in terms of cell proliferation in direct contact cultivations. Inoculation concentration in relation to the microtiter plate area: c = 10 400 cells cm^{-2}; N = 3. Data significance was assessed by the tukey test and is depicted as: *p < 0.05, **p < 0.01, ***p < 0.001

Janus kinase/Signal Transducer and Activator of Transcription (JAK/STAT) pathway activation for cell survival and proliferation. Therefore, we exploited the proliferation rate of 32D cells as a reliable readout to investigate PNIPAM-co-AAc microcarrier-mediated IL3 supply in normal cell culture. As a positive control, 32D cells were transfected with murine JAK2 harboring the oncogenic V617F (VF) mutation, which constitutively activates the JAK/STAT pathway, independent of IL3 stimulation. Additionally, the IL3 signaling cascade can be activated by IL3/IL3R interaction on the cell surface or the membrane of internalized vesicles during receptor recycling.[100]

Considering that GF immobilization by EDC-NHS coupling is irreversible and, therefore, leads to restriction of bioactivity to the particle surface, our first study focused on investigating the behavior of 32D cells cultured in direct contact with covalently functionalized microcarriers. The experimental setup is depicted in **Figure 6**A and was used to evaluate whether covalently bound IL3 can successfully support the survival of 32D cells *in vitro*. We determined the efficacy of IL3-presenting microcarriers by the difference in metabolic activity detected in an IL3-free (IL3-) medium, in which microcarrier-bound cytokine was the sole source of IL3, and an IL3-containing medium (IL3+), where the cytokine was externally supplied by Walter and Eliza Hall Institute (WEHI)-3B cell supernatant. Figure 6B.i presents the corresponding 3-(4,5-Dimethylthiazol-2-yl)-2,5-Diphenyltetrazolium Bromide (MTT) results for cultivation day 3 and 5, revealing a similar metabolic activity for EV and VF cells, independent of the cytokine source. Since EV cells are IL3-dependent, this similarity in metabolic activity in both medium types indicates that microcarrier-bound IL3 is presented in a bioactive form and supplied in sufficient quantity. However, in order to ensure that the survival of transfected 32D cells in IL3- medium is solely attributed to the IL3 functionalization, additional control experiments were conducted. First, proper cellular function was confirmed by cultivating 32D cells in the absence of microcarriers in both medium compositions. The results obtained from these microcarrier-free cultivations are depicted in Figure 6B.ii and demonstrate the expected lower metabolic activity of EV cells in IL3- medium compared to IL3+ medium. Second, 32D cells were cultured in direct contact with non-functionalized microcarriers. The corresponding data is presented in Figure 6B.iii and shows a similar metabolic behavior as observed in the absence of microcarriers, which excludes potential effects of the bare hydrogel on cell survival. Combining these findings with the data of our positive control group, which demonstrated comparable metabolic activity of VF cells in

each experimental subset, our studies conclude that PNIPAM-co-AAc microcarriers can be functionalized with active GF via EDC-NHS coupling.

However, since the NHS esters produced during priming are only meta-stable and, as such, are gradually hydrolyzed during the functionalization reaction, EDC-NHS coupling always leads to a certain percentage of unreacted carboxylic acids within the hydrogel. These residual groups generate a negative gel charge above a pH of 4.2 and can lead to electrostatic binding of IL3, which exhibits an iP of 8.3 and, hence, a positive charge at the reaction pH of 6.0. Consequently, it is realistic to assume that a certain fraction of the GF functionalization is caused by charge interactions between the hydrogel and cytokine rather than covalent coupling by EDC-NHS. To verify this hypothesis, we performed cultivations in which cells and microcarriers were spatially separated by transwell inserts, as depicted in Figure 6C. In this experimental setup, EV cells cannot interact with covalently bound GF, and potential cell survival must be related to the dissociation of adsorbed IL3 from the microcarriers. Figure 6D.i presents the metabolic activity of EV cells measured at cultivation days 3 and 5 for samples containing microcarriers functionalized via EDC-NHS coupling (MC-IL3-C) and compares it to the metabolic activity detected in specimen comprising microcarriers adsorptively coated with IL3 in the absence of EDC-NHS (MC-IL3-A). The corresponding graph shows similar metabolic values irrespective of the crosslinker's presence during the functionalization reaction for both cultivation days. This result indicates the dissociation of IL3 from both covalently and adsorptively functionalized microcarriers and, therefore, confirms our hypothesis that covalent EDC-NHS coupling was accompanied by transient electrostatic adsorption. Unlike wells containing cytokine-loaded particles, our negative controls comprising of EV cells cultivated in the absence of microcarriers (No MC) and the presence of non-functionalized microcarriers (MC-NF) showed significantly lower metabolic activity as expected during IL3 deprivation. Again, secondary influences on the metabolic activity can be excluded based on the results of our positive controls where IL3 is externally supplied by WEHI-containing media, which are presented in Figure 6D.ii for all experimental subsets.

Although transwell cultivations successfully verified our initial hypothesis regarding a dual functionalization mechanism, the results do not provide any information on the ratio between covalently and adsorptively bound GF in the case of EDC-NHS coupling or whether chemical immobilization of IL3 occurs at all. Since initial efforts to remove electrostatically attached cytokine amounts from MC-IL3-Cs were unsuccessful according to IL3 enzyme-linked immunosorbent assays (ELISA), we speculate that potential differences between MC-IL3-Cs and MC-IL3-As might be detectable in long-term cultures in which IL3 is either readily internalized or degraded. Figure 6E shows the number of viable EV cells cultured in direct contact with MC-IL3-Cs and MC-IL3-As, which were reused for five successive cultivations at similar inoculation concentrations, each lasting for a total of 5 days. Our results suggest that MC-IL3-As can successfully support the survival of EV cells during the first two cultivation cycles by diffusive cytokine release before the cell number rapidly decreases from cycle 3 to 5, indicating the slow depletion of IL3. Although a similar trend is detected for MC-IL3-Cs, cell numbers were significantly elevated during cycles 3 and 4, implying a prolonged supply of IL3. Since covalent conjugation is known to improve the stability and persistence of GF,[101] the observation of elevated cell numbers in later cultivation cycles for microcarriers functionalized via EDC-NHS coupling is a strong indicator for the presence of covalently bound cytokines, which become detectable when electrostatically bound IL3 is diffusively released and readily internalized or gradually degraded. This degradation at cultivation conditions is measurable as a rapid decline in IL3 concentration for MC-IL3-A after 12 h of incubation by ELISAs, which are depicted in Figure S13 (Supporting Information) and compared to the release of vascular endothelial growth factor (VEGF) as a control. Considering that the dual functionalization mechanism is primarily related to the opposite charges of the carboxyl groups and IL3 at physiological pH, we hypothesize that the ratio between electrostatically and covalently bound protein generated during EDC-NHS coupling is substantially dependent on the iP of the protein and the pH applied during protein conjugation. This effect can theoretically be harnessed to block adsorptive interactions during EDC-NHS coupling by adjusting the pH value according to the iP of the bioactive component which would allow the covalent immobilization of plasma membrane bound GF in a first reaction step, followed by the adsorptive immobilization of internalized bioactive agents to the residual AAc groups in a second loading step. The higher number of cells for covalently bound GF was confirmed by another experiment, proving reproducibility (Figure S14, Supporting Information).

3. Conclusion

In this study, we report the fabrication of micrometer-sized hydrogel microcarriers by co-polymerizing PNIPAM and AAc in a droplet microfluidic chip at a production rate of 300 particles per minute. Contrary to commercially available microcarriers, these hydrogel beads closely mimic the natural ECM and feature substantial and independent adaptability regarding their particle properties. In this context, tensile tests revealed that variations in crosslinker concentration between 5 and 10 mol.% result in elastic moduli ranging from 4 to 14 kPa, closely imitating the mechanical properties of softer tissue regions. Zeta potential measurements demonstrated that an increase in the AAc co-monomer content from 0 to 20 mol.% leads to a decrease in the particle surface potential from –1 to –27 mV, thereby moderately dampening the temperature-induced syneresis by improving water retention. In addition to the benefits regarding bead hydration, our experiments showed that the presence of AAc also enables covalent functionalization of the hydrogel matrix with cell adhesive motifs and cell fate-modulating proteins by EDC-NHS coupling. We verified the general functionality of the reaction mechanism by conjugating fluorescent amine-containing LY to the particle-matrix. Moreover, we proved the bioactivity of coupled adhesive proteins, including FN, Col, and Gel in static microtiter-plate and dynamic STBR cultivations, in which L929 mouse fibroblast cells exclusively attached and grew on functionalized microcarriers. In terms of cell fate-modulating proteins, we applied the optimized reaction protocol to conjugate the cytokine IL3 to PNIPAM-co-AAc beads, which could successfully support the survival of IL3-dependent myeloblast-like 32D cells for 20 days as the sole source of cytokine. However, transwell insert-based experiments applying IL3-containing

hydrogel beads revealed that the immobilization of highly protonated proteins like IL3 by EDC-NHS coupling is not exclusively due to covalent bonding, but is partially facilitated by electrostatic adsorption. This dual functionalization mechanism closely mimics the natural functionality of GAGs and leads to two categories of immobilized protein: 1) irreversibly bound protein demonstrating enhanced stability and 2) physically adsorbed protein released during cultivation along the concentration gradient. While electrostatic GF immobilization enables the sustained delivery of internalized GF, covalent coupling could allow the reuse of our microcarriers and significantly reduce the costs of adherent cell cultivation for industrial and medical processes.

4. Experimental Section

Microfluidic Chip Fabrication: Microfluidic chips were fabricated by PDMS replica molding. To this end, a master mold was designed in the computer-aided design (CAD) software Autodesk Inventor 2022, and the resulting geometry was printed on a silicon wafer (MicroChemicals GmbH, 3 inch) using two-photon lithography. Prior to the printing process, the silicon wafer was activated in oxygen plasma (40 mL min^{-1}, 0.3 mbar, 60 W) for 30 s (TePla 100 Plasma System, PVA) and was spin-coated with 1.5 mL of a tetraethyl orthosilicate (TEOS) (Sigma Aldrich, 98%, 131903), 3-(mercaptopropyl)trimethoxysilane (MTS) (Sigma Aldrich, 95%, 175617), ethanol (Sigma Aldrich, 51976), water mixture (1:2:1:1 vol.%) at 5000 rpm for 5 min. After curing at 55 °C overnight, the molding structures were printed onto the coated silicon wafer by dip-in laser lithography applying a multi-photon 3D printer (Photonic Professional GT, Nanoscribe GmbH) in combination with a 10X objective and IP-Q photo resin (Nanoscribe GmbH). The resulting master molds were subsequently developed for 10 min in propylene glycol methyl ether acetate (PEGMA) (Sigma –Aldrich, ⩾99.5%, 484431), cleaned in isopropanol (Sigma Aldrich, I9516), and post-cured under UV light (302 nm, 8 W) (Analytik Jena US) for at least 12 h. On the next day, the master molds were placed inside a Petri dish (Sigma Aldrich, P5731), and a 10:1 PDMS (Sylgard184, DowCorning) to curing agent mixture was poured onto the master mold. After curing at 50 °C for 12 h, the PDMS structures were removed from the mold using a scalpel, and channel in- and outlets were incorporated via a biopsy puncher (EMS, Rapid-Core 0.75 mm). The processed PDMS slabs were finally cleaned for 5 min in isopropanol within a sonicator bath (xtra TT, Elmasonic), dried in a desiccator for at least 1.5 h, treated in oxygen plasma (40 mL min^{-1}, 0.3 mbar, 60 W) for 60 s (TePla 100 Plasma System, PVA), and bonded to microscopy glass slides. Low-density polyethylene tubing (0.86 mm ID, 1.52 mm OD, Smiths Medical Portex LDPE) was inserted into the punch holes to connect the PDMS chips to the respective fluid compartments. The dimensions of the microfluidic chip utilized for microcarrier fabrication are presented as technical drawing in Figure S15 (Supporting Information).

Miniaturized Stirred-Tank Bioreactor: The STBR components were either directly adopted as STL files from Romero-Morales et al.[95] or were constructed in the computer-aided design (CAD) software Autodesk Inventor 2022. The stirrers were manufactured by a Form 3+ printer (formlabs) in combination with the corresponding high temp resin (formlabs, RS-F2-HTAM-02) and were thoroughly cleaned in isopropanol and DI water before usage. All other reactor components were produced by a polyjet 3D printer (Objet Eden 260V, Stratasys) in combination with the photopolymer RGD525 (Stratasys) and the support material SUP 705 (Stratasys), which was applied to support all internal structures during fabrication. The support material was later removed by mechanical ablation and dissolution in a 1M NaOH solution for at least 12 h. The STBR was finally assembled from the 3D printed parts, an electric motor (Greartisan DC 12V), plastic plain bearings (Conrad Electronic, JFM-0608-06), a Raspberry Pi 4 Model B, a touchscreen display (SunFounder, CN0199), spacer bolts (Bürklin GmbH & Co KG, M3 35 mm 18H184, M3 45 mm 18H188), and a motor bridge (Conrad Electronic, 1573541-62). The graphical user interface was programmed in Python version 3.8.2.

Computational Fluid Dynamics Simulation: The hydrodynamic conditions during cell cultivation were simulated using the frozen rotor study provided by Comsol Multiphysics 6.1 as a function of the stirrer type. The turbulent behavior was described by the k-ω-model, using the k-ϵ-model model as a starting point for better convergence. The mesh independence was ensured for both simulations, and the corresponding studies are presented in Figure S16 (Supporting Information). Both simulations featured approximately 2.8 million tetrahedral elements for the bulk phase and 0.35 million prisms for the boundary conditions.

Microcarrier Synthesis: The desired amounts of N-isopropylacrylamide (NIPAM, Sigma Aldrich, 731129), acrylic acid (AAc, Sigma Aldrich, 147230), N,N-methylenbis-(acrylamide) (BIS, Sigma Aldrich, 146072), and 13 mg mL^{-1} Lithium-Phenyl-2,4,6-trimethylbenzoylphosphinate (LAP, Sigma Aldrich, 900889) were dissolved in a mixture of 73.3 vol.% high-performance liquid chromatography (HPLC) grade water, 16.7 vol.% Poloxamer 188 (ThermoFisher Scientific, 24040032), and 10 vol.% glycerol (Sigma Aldrich, G6279). The resulting monomer solution was injected into a microfluidic droplet generator chip using an OB1 MK3+ flow controller (Elveflow), where the solution was emulsified in a continuous silicon oil (AR 20, Sigma Aldrich, 10836) phase. The generated W/O droplets were subsequently polymerized by exposure to 365 nm UV light (Analytik Jena US, 8 W) for 15 s and were collected in a reaction tube (Eppendorf). The solidified microcarriers were finally purified in isopropanol (Sigma Aldrich, I9516) for 3 d on a roller mixer before being transferred into a 70 vol.% ethanol (Sigma Aldrich, 51976) in DI water solution, in which they were sterilized for at least 1 d.

Protein Functionalization: A 2-(N-morpholino)ethanesulfonic acid (MES) buffer solution (50 mM, pH 5)(Sigma Aldrich, BioXtra ⩾99.0%, 69892) was prepared and steam-sterilized at 121 °C for 20 min (SystecTM VX-95). Microcarriers were sedimented by gravity, and the supernatant was aspirated. The microcarrier pellet was subsequently washed 3x in 50 mL of MES buffer solution (50 mM, pH 5) on a roller mixer for 30 min each. During the washing procedure, 0.4 M 1-ethyl-3-(3-dimethylaminopropyl)carbodiimide hydrochloride (EDC) (Thermofisher Scientific, 22980) and a 0.4 M N-Hydroxysuccinimid (NHS) (Sigma Aldrich, 130672) solutions were prepared in MES buffer (50 mM, pH 5) and were combined to a 0.2 M EDC/NHS mixture. For priming, 1.5 mL of 0.2 M EDC/NHS solution was added to 100 µL of microcarrier suspension, and the mixture was incubated at room temperature on a roller mixer for 20 min. After the priming reaction, the microcarriers were washed 2x in 1.5 mL of MES buffer solution (50 mM, pH 5) before being exposed to 1 mL of the desired protein solution on a roller mixer for 5 h. The functionalized microcarriers were finally washed 2× in 1.5 mL of protein solvent and at least 5× in 1.5 mL cell culture medium until the phenol red pH indicator suggested a stable pH of 7. Adsorptively functionalized samples were subject to an identical protocol while skipping the priming reaction. Fibronectin (Sigma Aldrich, 10838039001) and gelatin (Sigma Aldrich, G9391) were dissolved in pH 5 MES buffer at a concentration of 0.3 mg mL^{-1}, collagen (Sigma Aldrich, 11179179001) was dissolved in absolute ethanol (Sigma Aldrich, 51976) at a concentration 0.3 mg mL^{-1}, and recombinant murine interleukin-3 (PeproTech, 213-13) was dissolved in pH 6 MES buffer at a concentration of 0.1 mg/ml.

Scanning Electron Microscopy: Microcarriers suspended in isopropanol were dried in a desiccator for 3 d. The resulting samples were subsequently fixated on a sample holder using double-sided tape and were imaged applying a TM 3030Plus tabletop electron microscope at an accelerating voltage of 15 kV and a working distance of 5–10 mm.

Fourier Transform Infrared Spectroscopy: Microcarriers suspended in DI-water were frozen in liquid nitrogen and freeze-dried to generate a powder. The powder was subsequently pelleted on the Fourier Transform Infrared (FTIR) crystal by applying the corresponding stamp, and the samples were measured using a PerkinElmer Spectrum 3 FTIR spectrometer.

Zeta-Potential Measurements: For zeta-potential measurements, a Zetasizer Nano ZS (Malvern Panalytical) was applied. Considering its particle diameter limit of 5 µm, appropriately sized samples had to be synthesized by emulsion polymerization. To this end, 10 µL of monomer solution were

added to 100 µL of silicone oil. Subsequently, the two phases were emulsified by 20 s of shaking and the resulting emulsion was polymerized by 2 min of UV light exposure. After polymerization, the particle samples were purified twice in 700 µL of isopropanol by centrifuging (Hettich MIKRO 200R) at 15 000 g for 1 min. The obtained pellets were re-suspended in 400 µL of isopropanol before being size-separated by centrifugation at 3000 g for 10 s. Finally, 250 µL of upper liquid level supernatant was transferred to a fresh reaction tube, pelleted at 15 000 g for 5 min, washed twice in 400 µL of DI water at 15 000 g for 5 min, and stored at 4 °C until usage. For zeta potential measurement, 100 µL of the final suspension were diluted in 1 mL DI water. The resulting dilution was injected into a DTS1070 capillary cell (Malvern) and was measured at a temperature of 20 °C and an equilibration time of 180 s.

Tensile Measurements: For the tensile tests, 20 mm x 10 mm x 1 mm (L x B x H) hydrogel flat films were prepared by UV polymerization. To this end, 250 µL of polymer solution per film were pipetted into the corresponding mold, which was designed in Autodesk Inventor Professional 2022 and 3D printed (Objet Eden 260V, Stratasys) applying VeroClear RGD 810 (Stratasys) in combination with SUP 705 (Stratasys) support material. After filling, the mold was closed with microscopy slides and was exposed to 365 nm UV (Analytik Jena US, 8 W) light for 2.5 min from each side to achieve fully polymerized hydrogel films. Tensile tests were conducted using a custom build laboratory setup comprising of a micro-manipulator linear arm (MM33, Märzhäuser Wetzlar GmbH & Co. KG, Germany), a stepper motor (NEMA 17, Stepperonline), and a high precision scale (Mettler Toledo, Switzerland). Wet hydrogel films were immobilized between the linear arm and the scale via clamps, and the films were stretched until failure at a drawing speed of 0.2 mm/s. During the measurement, strain and mass were recorded by a self-written python script.

Nanoindentation Measurements: TC-treated 24-microtiter plates were coated with a poly-l-lysine solution (Sigma Aldrich, P4707) by droplet evaporation. Subsequently, PNIPAM-co-AAc particles were pipetted into the microtiter plate and sedimented for 10 min. The samples were washed four times in Milli-Q water to remove solvent residues and loose particles before measuring the remaining specimen with a Optics11Life Pavone Nanoindentation System, which was equipped with a spherical probe featuring a tip radius of 11 µm. Samples containing 5 mol.% BIS were measured in the displacement mode. The samples were first detected by the "find surface" option. Subsequently, the probe was raised to 50 µm above the detected value to guarantee the absence of sample contact before measurement. The probe approach speed was set to 1 000 nm s^{-1}, the retraction speed to 10 000 nm s^{-1}, and the displacement was adjusted to 80 000 nm. The resulting data was fit from 0 to 10 000 nm to ensure a sufficient R^2 value. Samples containing 6.8 mol.% and 10.0 mol.% BIS were measured in the indentation mode. The contact threshold was adjusted to 0.015, the approach speed to 1 000 nm s^{-1}, and the retraction speed to 30 000 nm s^{-1}. The measurement data was fit from 0 to 1 000 nm to guarantee for compliance with the Hertz contact model and sufficient R^2 values.

Thermo-Responsiveness Measurements: Microcarriers were added into a sub-compartment of a 6-well microtiter plate containing 10 mL of DI water. A heating stage (Okolab H401-T-Controller) was mounted onto a brightfield microscope (DM IL LED, Leica) and the corresponding temperature sensor was inserted into the compartment. With a set temperature of 60 °C, the microcarriers were subsequently heated to 40 °C. For determining the microcarrier's thermo-responsiveness, the heating process was recorded with a frame rate of 1 fps. The resulting image stack was finally imported into the software ImageJ, where it was converted into 8-bit images and treated with a bandpass filter. Color thresholding was applied to achieve distinct borders between the microcarriers and the background. The change in particle area was determined by ImageJ's analyze particle function.

Cell Maintenance: L929 mouse fibroblast cells (Sigma Aldrich, 85011425) were cultured in Gibco™ Roswell Park Memorial Institute (RPMI) 1640 medium (Fisher Scientific, 11530586) supplemented with 10% fetal bovine serum (FBS) (BH Biowest, 5181) and 1% penicillin/streptomycin (P/S) (Thermofisher Scientific, 15140). The cells were subcultured upon reaching 85% confluency and the passage number was restricted to a maximum of 30 subcultures. 32D empty vector (EV) and JAK2 V617F (VF) cells were established as previously described by Schubert et al.[102]. Both cell lines were cultured in Gibco™ RPMI 1640 medium supplemented with 10% FBS (Pan-Biotec, P30-3306) and 1% P/S. WEHI supernatant (10%) served as IL3 source for culturing 32D EV cells. Cells were kept at a seeding density of 10^6 cells mL and split every 3–4 days. The environmental culture conditions were maintained at 37 °C, 5% CO_2, and a humidity of 95%.

Cytotoxicity Assay: Microcarrier cytotoxicity was assessed by comparing the rate of cell proliferation in fresh medium with the rate of cell proliferation in leached medium by applying a tetrazolium salt-based cell proliferation kit II (XTT) (Sigma Aldrich, 11465015001). The leached medium was prepared by incubating a batch of 90 000 microcarriers in 10 mL of RPMI 1640 medium at 37 °C for 9 d. During the leaching period, the microcarriers were regularly re-suspended to ensure the proper transition of potentially toxic compounds into the medium. For the XTT assay, L929 mouse fibroblast cells were seeded in a tissue culture-treated 96 microplate at an inoculation concentration of 5 000 cells cm^{-2} and were maintained in either pure or leached medium for 9 d of cultivation. The medium was exchanged every 48 h with the respective medium type to ensure sufficient nutrient supply. For determining cell proliferation, the XTT reagent was prepared as described by the manufacturer and was mixed with Dulbecco's Modified Eagle Medium (DMEM) without phenol red (Thermofisher Scientific, 31053028) in a volume ratio of 1:2. Subsequently, the cell samples were washed with 100 µL phosphate-buffered saline (PBS, 1X) (Thermofisher, J61196.AP) followed by a 4 h long cultivation in 150 µL of reagent mixture at 37 °C, 5% CO_2, and a humidity of 95%. Finally, 100 µL of reagent mixture was transferred to a fresh 96 microplate, and the absorbance was measured using a microplate reader (Synergy HT, BioTek) at 450 and 630 nm. A blank measurement was performed using the reagent mixture incubated for 4 h in a 96 microplate in the absence of cells.

Microcarrier Cultivation of L929 Mouse Fibroblast Cells: The miniaturized bioreactor system was sterilized by washing in 70% ethanol (Sigma Aldrich, 51976) for 30 min, followed by a UV-sterilizing step for another 30 min. The microcarriers were pipetted into a sterile low-attachment 12 microplate (Thermofisher, Nunclon Sphera, 174931), and L929 mouse fibroblast cells were seeded at an inoculation concentration of 200 000 cells cm^{-2} in relation to the microplate's cultivation area. Subsequently, the medium level was adjusted to 4 mL, and an intermittent stirring sequence containing 12 loops of 1 min stirring at 30 RPM followed by 2 h without stirring was initiated to generate a homogeneous cell distribution. After seeding, the cell-laden microcarriers were either exposed to continuous stirring at 30 RPM for dynamic STBR cultivation or transferred into low-attachment 96 microplates (Thermofisher, Nunclon Sphera, 174927) for static cultivation, where the medium was exchanged every second day to ensure sufficient nutrient supply. The cultivation conditions were 37 °C, 5% CO_2, and a humidity of 95% independent of the type of experiment.

Determination of Cell Adhesion Rate: 200 000 L929 mouse fibroblast cells were mixed with 100 µL of FN-functionalized PNIPAM-co-AAc microcarriers in 1.5 mL Eppendorf tubes (d = 8.5 mm), which do not support cell adhesion. At certain time intervals (5 min, 10 min, 20 min, 40 min, 60 min), the supernatant from three different reaction tubes was separately collected and the microcarriers were washed with phosphate buffered saline (PBS) to remove non-adherent cells from the particle surface. The washing solution was collected for each reaction vial and added to the corresponding supernatant. Subsequently, the resulting cell suspensions were centrifuged at 300 rcf for 5 min and the collected cells were counted manually in a Neubauer chamber. The cell adhesion rate and the percentage of adherent cells were finally calculated according to the following equations:

$$r = \frac{n_i - n_{i-1}}{t_i - t_{i-1}} \quad (1)$$

$$p_{ad} = \left(1 - \frac{n_i}{n_0}\right) \cdot 100 \quad (2)$$

where r is the cell adhesion rate, n is the cell number, t is the time in min, p_{ad} is the percentage of adherent cells, n_0 is the total number of seeded cells, and i is the sample index.

Immunofluorescence Staining: Cells were stained for nuclei and plasma membranes by exposing the specimen to 4:1000 v/v 4,6-diamidino-2-phenylindole (DAPI) solution (Abcam, ab228549) for 10 min and 1:1000 v/v CellMask™ Orange (Thermofisher Scientific, C10045) for 30 min. Prior to labeling, all samples were fixed in 4% v/v paraformaldehyde (PFA) solution for 15 min, permeabilized in a 0.1% v/v Triton X-100 solution for 15 min, and rinsed thoroughly in PBS (1X) (Thermofisher, J61196.AP).

Enzyme-Linked Immunosorbent Assay: Microcarriers were loaded by incubation in 1.6 mL PBS (1X) (Thermofisher, J61196.AP) containing 400 pg mL^{-1} of either interleukin-3 (IL3) or vascular endothelial growth factor (VEGF) (Sigma Aldrich, SRP3182-10UG) on a roller mixer overnight. The loaded particles were washed 3x in PBS (1X) containing 0.05 wt.% bovine serum albumin (BSA) (Sigma Aldrich, A2153) and were finally incubated in an identical solution for 168 h at 37 °C. On sampling days, the specimens were homogenized by inverting the reaction tube. Subsequently, 120 µL of the microcarrier-free liquid was extracted and stored at –20 °C. The missing volume was refilled with 0.05 wt.% BSA in PBS (1X). For analysis, the frozen samples were thawed and treated with either a mouse IL3 enzyme-linked immunosorbent assay (ELISA) (abcam, ab222509) or a VEGF ELISA (abcam, AB222510-1001) kit according to the manufacturer's protocol. A Synergy HT plate reader (BioTek) was used to measure the sample absorption at 450 nm using path length correction, and the values were corrected by subtracting the absorption of pure diluent. The absorbance values were converted into concentrations by recording a calibration curve using the manufacturer's standards.

Microcarrier Cultivation of 32D Mouse myeloblast cells: For MTT assays, 32D EV and VF cells were seeded in 96-well plates (10 000 cells per well) with or without Walter and Eliza Hall Institute (WEHI) as a source of IL3 and in the presence or not of IL3 functionalized microcarriers (adsorbed or covalently bound) or non-functionalized microcarriers. The measurement of cell viability was performed 72 and 120 h later by adding 3-(4,5-Dimethylthiazol-2-yl)-2,5-Diphenyltetrazolium Bromide (MTT) reagent (Sigma-Aldrich) at a final concentration of 0.5 mg mL^{-1} to each well followed by incubation for 4 h at 37 °C and 5% CO_2 in humidified atmosphere. Measurement of absorption was conducted at a wavelength of 550 nm. For Transwell assays, 32D EV cells (30 000 cells per well) were seeded in a 24-well plate in 0.5 mL of 32D culture medium without WEHI supplementation. Functionalized microcarriers with covalently bound or adsorbed IL3 or non-functionalized were added on the upper part of a 0.4 m PET translucent Transwell (CellQart, 9320402) in 0.5 mL of 32D culture medium without WEHI supplementation. Cell proliferation was measured after 72 h by viable cell counting with a hemocytometer after Trypan Blue staining.

Statistics: The experimental data was analyzed with two-way Anova and tukey's mean comparison in OriginPro - Graphing & Analysis Software 2020 Software. An alpha value p less than 0.05 was considered statistically significant. The p values are indicated in the respective graphs.

Supporting Information

Supporting Information is available from the Wiley Online Library or from the author.

Acknowledgements

M.W. acknowledges DFG funding through the Gottfried Wilhelm Leibniz Award 2019 (WE 4678/12-1). This work was performed in part at the Center for Chemical Polymer Technology CPT, which is supported by the EU and the federal state of North Rhine-Westphalia (grant no. EFRE 30 00 883 02). M.A.S.T. and S.K. were funded by the German Research Foundation as part of the Clinical Research Unit CRU 344 (417911533). The authors thank the Institute of Biology II of RWTH Aachen University, Worringerweg 3, 52074 Aachen, Germany for providing the tensile tester and their valuable support during the measurements. The authors also thank Caroline Schmitz for her support in 3D printing.

Open access funding enabled and organized by Projekt DEAL.

Conflict of Interest

The authors declare that the research was conducted in the absence of any commercial or financial relationships that could be construed as a potential conflict of interest.

Data Availability Statement

The data that support the findings of this study are available from the corresponding author upon reasonable request.

Keywords

cell expansion, protein functionalization, PNIPAM, microcarrier, stimuli-responsive hydrogel

Received: May 23, 2024
Revised: October 16, 2024
Published online:

[1] K. Nilsson, *Biotechnol. Genet. Eng. Rev.* **1988**, *6*, 404.
[2] V. Bodiou, P. Moutsatsou, M. J. Post, *Front. Nutr.* **2020**, *7*, 10.
[3] A.-C. Tsai, T. Ma, *Bioreact. Stem Cell Biology: Methods Protocols* **2016**, 77.
[4] B. Li, X. Wang, Y. Wang, W. Gou, X. Yuan, J. Peng, Q. Guo, S. Lu, *J. Orthop. Transl.* **2015**, *3*, 51.
[5] M. A. Faynus, J. K. Bailey, B. O. Pennington, M. Katsura, D. A. Proctor, A. K. Yeh, S. Menon, D. G. Choi, J. S. Lebkowski, L. V. Johnson, D. O. Clegg, *Bioengineering* **2022**, *9*, 297.
[6] O.-W. Merten, *Philosoph. Trans. Roy. Soc. B: Biol. Sci.* **2015**, *370*, 20140040.
[7] Y. Hasebe, M. Yamada, R. Utoh, M. Seki, *J. Biosci. Bioeng.* **2023**, *135*, 417.
[8] N. K. Tripathi, A. Shrivastava, *Front. Bioeng. Biotech.* **2019**, *7*, 420.
[9] S. Kiesslich, A. A. Kamen, *Biotechnol. Adv.* **2020**, *44*, 107608.
[10] N. Xiang, X. Zhang, *Nat. Rev. Bioeng.* **2023**, 1.
[11] S. Derakhti, S. H. Safiabadi-Tali, G. Amoabediny, M. Sheikhpour, *Mater. Sci. Eng., C* **2019**, *103*, 109782.
[12] L. Chen, D. Guttieres, A. Koenigsberg, P. W. Barone, A. J. Sinskey, S. L. Springs, *Biomaterials* **2022**, *280*, 121274.
[13] X. Yan, K. Zhang, Y. Yang, D. Deng, C. Lyu, H. Xu, W. Liu, Y. Du, *Tissue Eng., Part C* **2020**, *26*, 263.
[14] D. E. Kehoe, D. Jing, L. T. Lock, E. S. Tzanakakis, *Tissue Eng., Part A* **2010**, *16*, 405.
[15] A. Kumar, B. Starly, *Biofabrication* **2015**, *7*, 044103.
[16] J. Rowley, E. Abraham, A. Campbell, H. Brandwein, S. Oh, *BioProcess Int.* **2012**, *10*, 7.
[17] M. S. Moritz, S. E. Verbruggen, M. J. Post, *J. Integr. Agric.* **2015**, *14*, 208.
[18] A. T. Lam, S. Reuveny, S. K.-W. Oh, *Stem Cell Res.* **2020**, *44*, 101738.
[19] D. E. Nogueira, C. A. Rodrigues, J. M. Cabral, in Methods in iPSC Technology, Elsevier, **2021**, pp. 163–185.
[20] F. Manstein, K. Ullmann, C. Kropp, C. Halloin, W. Triebert, A. Franke, C.-M. Farr, A. Sahabian, A. Haase, Y. Breitkreuz, M. Peitz, O. Brüstle, S. Kalies, U. Martin, R. Olmer, R. Zweigerdt, *Stem Cells Translat. Med.* **2021**, *10*, 1063.
[21] B. M. Davis, E. R. Loghin, K. R. Conway, X. Zhang, *SLAS TECHNOLOGY: Translating Life Sciences Innovation* **2018**, *23*, 364.
[22] S. Abbasalizadeh, M. R. Larijani, A. Samadian, H. Baharvand, *Tissue Eng., Part C* **2012**, *18*, 831.
[23] D. Egger, C. Tripisciano, V. Weber, M. Dominici, C. Kasper, *Bioengineering* **2018**, *5*, 48.

[24] J. Reiss, S. Robertson, M. Suzuki, *Int. J. Mol. Sci.* **2021**, *22*, 7513.
[25] A. L. Farris, A. N. Rindone, W. L. Grayson, *J. Mater. Chem. B* **2016**, *4*, 3422.
[26] K. P. Clapp, A. Castan, E. K. Lindskog, in *Biopharmaceutical processing*, Elsevier, **2018**, pp. 457–476.
[27] X.-Y. Chen, J.-Y. Chen, X.-M. Tong, J.-G. Mei, Y.-F. Chen, X.-Z. Mou, *Biotechnol. Lett.* **2020**, *42*, 1.
[28] C. Ferrari, F. Balandras, E. Guedon, E. Olmos, I. Chevalot, A. Marc, *Biotechnol. Prog.* **2012**, *28*, 780.
[29] I. Takahashi, K. Sato, H. Mera, S. Wakitani, M. Takagi, *Cytotechnology* **2017**, *69*, 503.
[30] R. Eibl, D. Eibl, R. Pörtner, G. Catapano, P. Czermak, G. Catapano, P. Czermak, R. Eibl, D. Eibl, R. Pörtner, *Cell and Tissue Reaction Engineering: With a Contribution by Martin Fussenegger and Wilfried Weber* **2009**, pp. 173–259.
[31] A. D. Dias, J. M. Elicson, W. L. Murphy, *Adv. Healthcare Mater.* **2017**, *6*, 1700072.
[32] A. Z. Unal, J. L. West, *Bioconjugate Chem.* **2020**, *31*, 2253.
[33] M. M. Rana, H. De la Hoz Siegler, *Polymers* **2021**, *13*, 3154.
[34] R. Begum, Z. H. Farooqi, S. R. Khan, *Int. J. Polym. Mater. Polym. Biomater.* **2016**, *65*, 841.
[35] E. P. Sproul, S. Nandi, C. Roosa, L. Schreck, A. C. Brown, *Adv. Biosyst.* **2018**, *2*, 1800042.
[36] S. Pawłowska, C. Rinoldi, P. Nakielski, Y. Ziai, O. Urbanek, X. Li, T. A. Kowalewski, B. Ding, F. Pierini, *Adv. Mater. Interfaces* **2020**, *7*, 2000247.
[37] I. Sanzari, E. Buratti, R. Huang, C. G. Tusan, F. Dinelli, N. D. Evans, T. Prodromakis, M. Bertoldo, *Sci. Rep.* **2020**, *10*, 6126.
[38] S. Li, W. Wang, W. Li, M. Xie, C. Deng, X. Sun, C. Wang, Y. Liu, G. Shi, Y. Xu, X. Ma, J. Wang, *Adv. Funct. Mater.* **2021**, *31*, 2102685.
[39] Y. Chen, Y. Gao, L. P. da Silva, R. P. Pirraco, M. Ma, L. Yang, R. L. Reis, J. Chen, *Polym. Chem.* **2018**, *9*, 4063.
[40] M. Zhang, G. Qing, C. Xiong, R. Cui, D.-W. Pang, T. Sun, *Adv. Mater.* **2012**, *25*, 749.
[41] Y. Chandorkar, A. Castro Nava, S. Schweizerhof, M. Van Dongen, T. Haraszti, J. Köhler, H. Zhang, R. Windoffer, A. Mourran, M. Möller, L. De Laporte, *Nat. Commun.* **2019**, *10*, 4027.
[42] S. Djeljadini, T. Lohaus, M. Gausmann, S. Rauer, M. Kather, B. Krause, A. Pich, M. Möller, M. Wessling, *Adv. Biosyst.* **2020**, *4*, 2000081.
[43] J. Zhang, Z. Cui, R. Field, M. G. Moloney, S. Rimmer, H. Ye, *Eur. Polym. J.* **2015**, *67*, 346.
[44] A. Tamura, J. Kobayashi, M. Yamato, T. Okano, *Biomaterials* **2012**, *33*, 3803.
[45] H. F. Darge, S.-H. Chuang, J.-Y. Lai, S.-Y. Lin, H.-C. Tsai, *Biotechnol. Bioeng.* **2021**, *118*, 4076.
[46] C.-F. J. Kuo, C.-J. Mei, C.-C. Huang, X.-T. Lin, T.-Y. Wu, H. F. Darge, S.-Y. Lin, H.-C. Tsai, *Eur. Polym. J.* **2023**, *195*, 112238.
[47] S. M. H. Dabiri, E. Samiei, S. Shojaei, L. Karperien, B. Khun Jush, T. Walsh, M. Jahanshahi, S. Hassanpour, D. Hamdi, A. Seyfoori, S. Ahadian, A. Khademhosseini, M. Akbari, *Small* **2021**, *17*, 2103192.
[48] X. Xu, Y. Liu, W. Fu, M. Yao, Z. Ding, J. Xuan, D. Li, S. Wang, Y. Xia, M. Cao, *Polymers* **2020**, *12*, 580.
[49] E. Han, S. S. Chen, S. M. Klisch, R. L. Sah, *Biophys. J.* **2011**, *101*, 916.
[50] K. Martineau, *Chinese J. Clin. Exp. Pathol.* **2021**, *11*, 2161.
[51] C. Frevert, T. Wight, in *Encyclopedia of Respiratory Medicine*, Academic Press, **2006**.
[52] T. Gan, Y. Guan, Y. Zhang, *J. Mater. Chem.* **2010**, *20*, 5937.
[53] J. Zhang, S. Yun, J. Bi, S. Dai, Y. Du, A. C. Zannettino, H. Zhang, *J. Mater. Chem. B* **2018**, *6*, 1799.
[54] E. Gojło, M. Smiechowski, A. Panuszko, J. Stangret, *J. Phys. Chem. B* **2009**, *113*, 8128.
[55] T. Si, Y. Wang, W. Wei, P. Lv, G. Ma, Z. Su, *React. Funct. Polym.* **2011**, *71*, 728.
[56] X.-Z. Zhang, D.-Q. Wu, C.-C. Chu, *J. Polym. Sci., Part B: Polym. Phys.* **2003**, *41*, 582.
[57] J. Grenier, H. Duval, F. Barou, P. Lv, B. David, D. Letourneur, *Acta Biomater.* **2019**, *94*, 195.
[58] M. V. Dinu, M. Přádný, E. S. Drăgan, J. Michálek, *Carbohydr. Polym.* **2013**, *94*, 170.
[59] I. Bružauskaitė, D. Bironaitė, E. Bagdonas, E. Bernotienė, *Cytotechnology* **2016**, *68*, 355.
[60] N. E. Zander, J. A. Orlicki, A. M. Rawlett, T. P. Beebe Jr, *J. Mater. Sci.: Mater. Med.* **2013**, *24*, 179.
[61] S. Cai, C. Wu, W. Yang, W. Liang, H. Yu, L. Liu, *Nanotech. Rev.* **2020**, *9*, 971.
[62] A. Khan, *Mater. Lett.* **2008**, *62*, 898.
[63] Y. K. Kim, E.-J. Kim, J. H. Lim, H. K. Cho, W. J. Hong, H. H. Jeon, B. G. Chung, *Nanoscale Res. Lett.* **2019**, *14*, 1.
[64] D. T. Butcher, T. Alliston, V. M. Weaver, *Nat. Rev. Cancer* **2009**, *9*, 108.
[65] X.-R. Yan, J. Li, X.-M. Na, T. Li, Y.-F. Xia, W.-Q. Zhou, G.-H. Ma, *Chin. J. Polym. Sci.* **2022**, *40*, 1080.
[66] L. Guillou, A. Babataheri, P.-H. Puech, A. Barakat, J. Husson, *Sci. Rep.* **2016**, *6*, 21529.
[67] A.-C. Tsai, R. Jeske, X. Chen, X. Yuan, Y. Li, *Front. Bioeng. Biotech.* **2020**, *8*, 640.
[68] W. Su, K. Zhao, J. Wei, T. Ngai, *Soft Matter* **2014**, *10*, 8711.
[69] M. Podewitz, Y. Wang, P. K. Quoika, J. R. Loeffler, M. Schauperl, K. R. Liedl, *J. Phys. Chem. B* **2019**, *123*, 8838.
[70] M. Yang, C. Liu, Y. Lian, K. Zhao, D. Zhu, J. Zhou, *Soft Matter* **2017**, *13*, 2663.
[71] A. A. Smith, C. L. Maikawa, H. L. Hernandez, E. A. Appel, *Polym. Chem.* **2021**, *12*, 1918.
[72] P. Narang, P. Venkatesu, *New J. Chem.* **2018**, *42*, 13708.
[73] C. Dionigi, Y. Piñeiro, A. Riminucci, M. Bañobre, J. Rivas, V. Dediu, *Appl. Phys. A* **2014**, *114*, 585.
[74] N. Oral, G. Basal, *J. Polym. Res.* **2023**, *30*, 34.
[75] H. Kawasaki, S. Sasaki, H. Maeda, *J. Phys. Chem. B* **1997**, *101*, 4184.
[76] R. A. Stile, W. R. Burghardt, K. E. Healy, *Macromolecules* **1999**, *32*, 7370.
[77] J. Zhang, L.-Y. Chu, Y.-K. Li, Y. M. Lee, *Polymer* **2007**, *48*, 1718.
[78] A. Burmistrova, M. Richter, M. Eisele, C. Üzüm, R. Von Klitzing, *Polymers* **2011**, *3*, 1575.
[79] S. A. Madison, J. O. Carnali, *Ind. Eng. Chem. Res.* **2013**, *52*, 13547.
[80] S. K. Vashist, *Diagnostics* **2012**, *2*, 23.
[81] E. N. Chiang, R. Dong, C. K. Ober, B. A. Baird, *Langmuir* **2011**, *27*, 7016.
[82] Z. Qu, H. Xu, H. Gu, *ACS Appl. Mater. Interfaces* **2015**, *7*, 14537.
[83] N. Guan, L. Liu, *Appl. Microbiol. Biotechnol.* **2020**, *104*, 51.
[84] J. Teixeira, F. Basit, H. G. Swarts, M. Forkink, P. J. Oliveira, P. H. Willems, W. J. Koopman, *Redox Biol.* **2018**, *15*, 394.
[85] L. Chen, C. Yan, Z. Zheng, *Mater. Today* **2018**, *21*, 38.
[86] E. Y. Liu, S. Jung, H. Yi, *Langmuir* **2016**, *32*, 11043.
[87] Z. Qu, K. Chen, H. Gu, H. Xu, *Bioconjugate Chem.* **2014**, *25*, 370.
[88] A. Gossart, K. G. Battiston, A. Gand, E. Pauthe, J. P. Santerre, *Acta Biomater.* **2018**, *66*, 129.
[89] K. K. Elineni, N. D. Gallant, *Biophys. J.* **2011**, *101*, 2903.
[90] N. D. Gallant, K. E. Michael, A. J. García, *Mol. Biol. Cell* **2005**, *16*, 4329.
[91] C. A. Reinhart-King, M. Dembo, D. A. Hammer, *Langmuir* **2003**, *19*, 1573.
[92] J. Wiebe, C. Dinsdale, *Life Sci.* **1991**, *48*, 1511.
[93] A. F. Davidson, C. Glasscock, D. R. McClanahan, J. D. Benson, A. Z. Higgins, *PloS one* **2015**, *10*, e0142828.
[94] M. A. Cooperstein, H. E. Canavan, *Biointerphases* **2013**, *8*, 1.
[95] A. I. Romero-Morales, B. J. O'Grady, K. M. Balotin, L. M. Bellan, E. S. Lippmann, V. Gama, *HardwareX* **2019**, *6*, e00084.

[96] L. H. Osaki, P. Gama, *Int. J. Mol. Sci.* **2013**, *14*, 10143.
[97] G. S. Schultz, A. Wysocki, *Wound Repair Regener.* **2009**, *17*, 153.
[98] S.-H. Kim, J. Turnbull, S. Guimond, *J. Endocrinology* **2011**, *209*, 139.
[99] D. Enriquez-Ochoa, P. Robles-Ovalle, K. Mayolo-Deloisa, M. E. Brunck, *Front. Bioeng. Biotech.* **2020**, *8*, 620.
[100] A. Nagamachi, J. Kikuchi, A. Kanai, Y. Furukawa, T. Inaba, *Haematologica* **2020**, *105*, e325.
[101] K. S. Masters, *Macromol. Biosci.* **2011**, *11*, 1149.
[102] C. Schubert, M. Allhoff, S. Tillmann, T. Maié, I. G. Costa, D. B. Lipka, M. Schemionek, K. Feldberg, J. Baumeister, T. H. Brümmendorf, N. Chatain, S. Koschmieder, *J. Hematol. Oncol.* **2019**, *12*, 1.